Journal of Neuroscience Methods 382 (2022) 109693

Contents lists available at ScienceDirect

Journal of Neuroscience Methods

journal homepage: www.elsevier.com/locate/jneumeth

Source-based artifact-rejection techniques for TMS–EEG

Tuomas P. Mutanen [a,*], Johanna Metsomaa [a,b], Matilda Makkonen [a], Giuseppe Varone [c], Laura Marzetti [c,d], Risto J. Ilmoniemi [a]

[a] Department of Neuroscience and Biomedical Engineering, Aalto University School of Science, Finland
[b] Department of Neurology & Stroke and Hertie Institute for Clinical Brain Research, University of Tübingen, Germany
[c] Department of Neuroscience, Imaging and Clinical Sciences, University of Chieti-Pescara, Italy
[d] Institute for Advanced Biomedical Technologies, University of Chieti-Pescara, Italy

ARTICLE INFO

Keywords:
Transcranial magnetic stimulation
Electroencephalography
Artifact signal
Noise
Signal space
Source space

ABSTRACT

Neuronal electroencephalography (EEG) signals arise from the cortical postsynaptic currents. Due to the conductive properties of the head, these neuronal sources produce relatively smeared spatial patterns in EEG. We can model these topographies to deduce which signals reflect genuine TMS-evoked cortical activity and which data components are merely noise and artifacts.

This review will concentrate on two source-based artifact-rejection techniques developed for TMS–EEG data analysis, signal-space-projection–source-informed reconstruction (SSP–SIR), and the source-estimate-utilizing noise-discarding algorithm (SOUND). The former method was designed for rejecting TMS-evoked muscle artifacts, while the latter was developed to suppress noise signals from EEG and magnetoencephalography (MEG) in general.

We shall cover the theoretical background for both methods, but most importantly, we will describe some essential practical perspectives for using these techniques effectively. We demonstrate and explain what approaches produce the most reliable inverse estimates after cleaning the data or how to perform non-biased comparisons between cleaned datasets. All noise-cleaning algorithms compromise the signals of interest to a degree. We elaborate on how the source-based methods allow objective quantification of the overcorrection. Finally, we consider possible future directions. While this article concentrates on TMS–EEG data analysis, many theoretical and practical aspects, presented here, can be readily applied in other EEG/MEG applications.

Overall, the source-based cleaning methods provide a valuable set of TMS–EEG preprocessing tools. We can objectively evaluate their performance regarding possible overcorrection. Furthermore, the overcorrection can always be taken into account to compare cleaned datasets reliably. The described methods are based on current electrophysiological and anatomical understanding of the head and the EEG generators; strong assumptions of the statistical properties of the noise and artifact signals, such as independence, are not needed.

1. Introduction

In the harsh electromagnetic environment during transcranial magnetic stimulation (TMS), electroencephalography (EEG) signals often suffer from artifact and noise contamination. Recently, there has been an exciting development in signal-analysis techniques that utilize physiological modeling of the cortical EEG generators to distinguish intracranial current sources of interest from various extracranial disturbances (Mutanen et al., 2016, 2018; Vosskuhl et al., 2020). Unlike some other popular cleaning methods, such as independent component analysis (ICA) (Korhonen et al., 2011; Rogasch et al., 2014), source-based methods are not based on as strict statistical assumptions. Hence, they provide a valuable set of TMS–EEG preprocessing tools when, *e.g.*, artifacts cannot be assumed independent of neuronal deflections.

A spatial-filtering method, the signal-space projection (SSP), was originally suggested by Mäki and Ilmoniemi (2011) for rejecting TMS-evoked muscle artifacts. A related, but less-refined, purely principal-component-analysis-based technique was later proposed by ter Braack et al. (2013). However, spatial filtering also modified the voltage patterns of the neuronal EEG signals across the sensors, hindering the visual interpretation of the cleaned data. Source-informed reconstruction (SIR) was developed to recover the original spatial patterns of the neuronal signals, uncovered from muscular artifacts (Mutanen et al., 2016). Following closely the logic of SIR, the source-estimate-utilizing noise-discarding algorithm (SOUND) was developed to detect and suppress noise in EEG and magnetoencephalography (MEG) au-

* Correspondence to: Department of Neuroscience and Biomedical Engineering, Aalto University School of Science, P.O. Box 12200, FI-00076 AALTO, Finland.
E-mail address: tuomas.mutanen@aalto.fi (T.P. Mutanen).

https://doi.org/10.1016/j.jneumeth.2022.109693
Received 14 October 2021; Received in revised form 14 August 2022; Accepted 25 August 2022
Available online 31 August 2022

tomatically (Mutanen et al., 2018). Since then, both SSP–SIR and SOUND have gradually gained more and more popularity among the TMS–EEG community (see *e.g.*, Bagattini et al., 2019; Ramakrishnan et al., 2019; Bortoletto et al., 2021; Grasso et al., 2021; Pievani et al., 2021; Mancuso et al., 2021). However, so far, the different aspects of source-based methods have not been covered in a comprehensive review.

This review is meant as a short handbook that facilitates the effective use of source-based methods in processing TMS–EEG data. We attempt to answer many of the practical questions that have been raised since the original publications, such as the best order of applying SOUND and SSP–SIR in preprocessing TMS–EEG data or how to combine inverse estimation with these methods optimally. We also communicate some significant technical innovations, which have been made over the years but have not been formally documented. Occasionally, we include simple simulations to effectively communicate certain aspects and ideas. The paper mainly concentrates on SSP–SIR and SOUND, but other closely related techniques are briefly covered as well. First, we will explain the fundamental physical background theory of source-based methods and derive SSP–SIR and SOUND from the basic principles. We shall next raise some critical practical perspectives when applying these methods. Finally, we will review the recent technical advances and shed light on the potential future directions.

2. Physiological and physical background

The prime generators in the brain for the EEG signals are neuronal populations that drive synchronous postsynaptic currents (PSCs) (Nunez et al., 2006). PSCs are the flow of ions within dendritic shafts towards the cell soma. For excitatory or inhibitory PSCs, the current consists of positive or negative ions, respectively. This transmission of ions causes local imbalances of net charge, giving rise to an electric field $\mathbf{E}(\mathbf{r})$ that drives so-called volume currents $\mathbf{J}^{\mathrm{V}}$ in the head. Thus, the total current density $\mathbf{J}(\mathbf{r})$ at location $\mathbf{r}$ can be written as:

$$\mathbf{J}(\mathbf{r}) = \mathbf{J}^{\mathrm{P}}(\mathbf{r}) + \mathbf{J}^{\mathrm{V}}(\mathbf{r}) = \mathbf{J}^{\mathrm{P}}(\mathbf{r}) + \sigma(\mathbf{r})\mathbf{E}(\mathbf{r}), \tag{1}$$

where $\mathbf{J}^{\mathrm{P}}(\mathbf{r})$ is the primary current density, *i.e.*, the net PSC at $\mathbf{r}$, and $\sigma(\mathbf{r})$ is the conductivity. It is noteworthy that in the presence of some $\mathbf{J}^{\mathrm{P}}$ in the brain, $\mathbf{E}$ is distributed across the whole head, not only in the locations of $\mathbf{J}^{\mathrm{P}}$.

EEG signal of channel i, $y_i(t)$ is the potential difference between an active electrode i and the reference electrode ref, which can be written as a path integral across the volume-current-related electric field along the scalp:

$$y_i(t) = V_{i,\mathrm{ref}}(t) = \int_{\mathrm{ref}}^{(i)} \mathbf{E}(\mathbf{r},t) \cdot d\mathbf{l}. \tag{2}$$

Because the electric field $\mathbf{E}$, related to the volume currents, is driven by the total primary current distribution $\mathbf{J}^{\mathrm{P}}$ in the whole head, the signal of channel i can be written as:

$$y_i(t) = \int_{V'} \mathbf{l}_i(\mathbf{r}') \cdot \mathbf{J}^{\mathrm{P}}(\mathbf{r}',t)\mathrm{d}V', \tag{3}$$

where $\mathbf{l}_i(\mathbf{r})$ is the so-called lead-field that describes the sensitivity of channel i to primary currents at $\mathbf{r}$. Fundamentally, $\mathbf{l}_i$ is determined by the locations of the i and ref channels on the scalp, the conductivity structure of the head, and the locations and orientations of the primary currents.

By describing the cortical $\mathbf{J}^{\mathrm{P}}$ distribution in terms of discretized equivalent sources, we can write the whole EEG recordings with matrix notation as:

$$\mathbf{Y}(t) = \mathbf{L}\mathbf{J}(t), \tag{4}$$

where the element L_{ij} describes the sensitivity of channel i to the cortical equivalent source j. The rows of $\mathbf{L}$ describe the sensitivity profiles of different EEG sensors to all the possible cortical sources. The

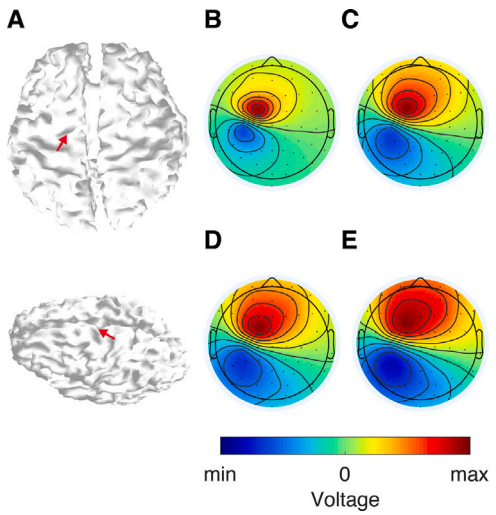

Fig. 1. The conductive properties of the head affect the spread of the ohmic volume currents, and thus, the resulting EEG topographies. **A**: The red arrow indicates the location and orientation of the simulated focal postsynaptic current source located on the precentral gyrus. **B**: The spread of the voltage pattern, resulting from the focal current source, when assuming that the whole head is a homogeneous, conductive body, surrounded by a vacuum (effectively the same as air). **C**: The corresponding voltage patterns when assuming a three-layer model (brain, skull, and scalp) and a 1:25 ratio in the conductivities between brain/scalp and skull **D**: The corresponding voltage patterns when assuming the same three-layer model and a 1:50 ratio in the conductivities between brain/scalp and skull. **E**: Including CSF in the model spreads the conductivity patterns even further. The simulations here were performed in MATLAB. The magnetic resonance images were segmented into tissue boundaries using SIMNIBS (Thielscher et al., 2015) whereas the lead fields were computed with the linear collocation BEM solver formulated using isolated source approach (Stenroos and Nummenmaa, 2016).

columns of $\mathbf{L}$, on the other hand, describe the scalp voltage patterns, or topographies, generated by individual, focal cortical current sources. In practice, the neuronal lead-field matrix $\mathbf{L}$ can be constructed by placing the equivalent current dipoles, portraying focal primary current sources, to plausible brain locations and by computing the EEG topographies resulting from each dipole. The geometrical information of the head is segmented from magnetic-resonance images, and the final calculations can be based on boundary-element methods (Stenroos and Nummenmaa, 2016) or finite-element methods (Ziegler et al., 2014).

However, Eq. (4) only holds for ideal measurements. In practice, we always measure also artifact and noise signals. We can include them in our linear model:

$$\mathbf{Y}(t) = \mathbf{L}\mathbf{J}(t) + \mathbf{M}_{\mathrm{A}}\mathbf{S}_{\mathrm{A}}(t) + \mathbf{M}_{\mathrm{N}}\mathbf{S}_{\mathrm{N}}(t), \tag{5}$$

where $\mathbf{M}_{\mathrm{A}}$ and $\mathbf{M}_{\mathrm{N}}$ are the artifact- and noise-mixing matrices, and $\mathbf{S}_{\mathrm{A}}$ and $\mathbf{S}_{\mathrm{N}}$ are the artifact- and noise-signal matrices, respectively. The columns of mixing matrices hold the topographies of different contaminating signal components, whereas the rows of signal matrices contain the time courses of the corresponding components.

Due to the conductive properties of the head, neuronal EEG signals are dominated by topographical patterns with low spatial specificity. Because the skull has low conductance, only a small portion of the volume currents travel across it and reach the scalp. The majority of the current travels through the brain tissue or the cerebrospinal fluid (CSF). Furthermore, most of the volume currents that reach the skin tend to travel extended distances through the well-conducting scalp before passing again through the skull. Together, these effects extensively smear the neuronally-generated electric fields on the scalp and, thus, the topographies (see Fig. 1 for illustrations). On the other hand, artifact and noise sources are generally created extracranially and can have topographies at higher spatial frequencies. This means that the column vectors of $\mathbf{L}$ can differ significantly from the column vectors of the artifact- and noise-mixing matrices. Broadly, the goal of

source-based methods is to utilize the discrepancy between the neuronal and noise and artifact topographies to design such spatial filters $\mathbf{W}_{\text{filter}}$ that approximately satisfy

$$\mathbf{W}_{\text{filter}}\mathbf{Y}(t) = \mathbf{W}_{\text{filter}}\mathbf{L}\mathbf{J}(t) + \mathbf{W}_{\text{filter}}\mathbf{M}_{\text{A}}\mathbf{S}_{\text{A}}(t) + \mathbf{W}_{\text{filter}}\mathbf{M}_{\text{N}}\mathbf{S}_{\text{N}}(t) \approx \mathbf{W}_{\text{filter}}\mathbf{L}\mathbf{J}(t)\,. \tag{6}$$

Fig. 1 shows how considerably the conductive properties of the head affect the spread of the volume currents and thus the resulting voltage patterns. Although the exact conductivities are not perfectly known (Vorwerk et al., 2019), we can model the qualitative effects of the poorly conducting skull and well-conducting CSF. Even focal cortical current sources produce voltage patterns that are considerably spread. Hence, neuronal EEG signals are, on average, highly correlated across the EEG sensors. While this low spatial specificity can hamper the unmixing of EEG signals into the original neuronal components, we can exploit the high correlation of neuronal EEG signals when separating them from extracranial sources.

3. SSP–SIR method

The most trivial way to clean data from artifacts and noise is to reject the contaminated sensor signals from further analysis. Indeed, this is a powerful and intuitive approach when the disturbances are confined to only a few so-called bad channels. Rejecting a channel decreases the dimensionality of the data by one. For instance, after discarding two channels from a 60-channel EEG dataset, we can theoretically estimate maximally 58 degrees of freedom of the cortical activity (57 in average reference). That said, this approach is not feasible if the artifact is simultaneously present in several channels. However, even if artifact signals are present in multiple channels, they could be described with a few spatial topographies that vary in amplitude over time but not in their spatial shape.[1] If this is the case, one can still reduce the dimensionality of the data only moderately to remove the unwanted signals.

When inspecting the linear model for our recordings (Eq. (5)), we can see that the spatial patterns of the different signal components, *i.e.*, the columns of the lead field and mixing matrices, are time-invariant. However, specific signal components might be more pronounced at certain times or certain frequencies, manifested in the time courses $\mathbf{J}(t)$, $\mathbf{S}_{\text{A}}(t)$, and $\mathbf{S}_{\text{N}}(t)$. The idea of signal-space projection (SSP) is to utilize these temporal variations to identify the artifact topographies that can be projected out (Uusitalo and Ilmoniemi, 1997; Mäki and Ilmoniemi, 2011). For instance, if we know that a certain time interval or frequency range includes almost only artifacts, we can use this portion of data to estimate the artifact-topographies to be rejected out.

Here, we concentrate on rejecting TMS-evoked muscle artifacts, which overlap in time with the early cortical reactions to TMS (Mutanen et al., 2013). However, brain activity mainly manifests in EEG in frequencies below 100 Hz (Buzsáki and Draguhn, 2004), while muscle activity shows a broadband response (Mäki and Ilmoniemi, 2011; Mutanen et al., 2016). Thus, by high-pass filtering the TMS–EEG data, we can highlight muscle activity:

$$\begin{aligned} H\big(\mathbf{Y}(t)\big) &= \mathbf{L}H\big(\mathbf{J}(t)\big) + \mathbf{M}_{\text{A}}H\big(\mathbf{S}_{\text{A}}(t)\big) + \mathbf{M}_{\text{N}}H\big(\mathbf{S}_{\text{N}}(t)\big) \\ H\big(\mathbf{Y}(t)\big) &\approx \mathbf{M}_{\text{A}}H\big(\mathbf{S}_{\text{A}}(t)\big) + \mathbf{M}_{\text{N}}H\big(\mathbf{S}_{\text{N}}(t)\big) \\ H\big(\mathbf{Y}(t)\big) &= \mathbf{U}\mathbf{S}\mathbf{V}^{\text{T}} \end{aligned}\,, \tag{7}$$

where $H(\cdot)$ stands for a high-pass filter and $\mathbf{U}\mathbf{S}\mathbf{V}^{\text{T}}$ is the singular value decomposition of the high-pass filtered data. If we can assume that the noise is relatively uncorrelated, the topographies (column vectors of $\mathbf{U}$) corresponding to the k most significant singular values should explain most of the muscle artifacts. Note that non of the individual vectors $\mathbf{U}_k$ $k = 1, 2, \ldots, k$ need to correspond to an underlying muscle-artifact component exactly. It suffices that a linear combination of the singular vectors explains the actual artifact topographies. *I.e.*, we say that the singular vectors span the muscle-artifact subspace.

If the k-most significant singular vectors $\mathbf{U}_k$ span the artifact-signal subspace, we can write the spatial filter $\mathbf{W}_{\text{SSP}}$ for muscle-artifact removal as:

$$\begin{aligned} \mathbf{U}_k\mathbf{S}_k\mathbf{V}_k^{\text{T}} &\approx \mathbf{M}_{\text{A}}H\big(\mathbf{S}_{\text{A}}(t)\big) \\ \mathbf{W}_{\text{SSP}} &= \mathbf{I} - \mathbf{U}_k\mathbf{U}_k^{\text{T}}\,, \end{aligned} \tag{8}$$

leading to $\mathbf{W}_{\text{SSP}}\mathbf{M}_{\text{A}} \approx 0$. Hence, we can write the muscle-artifact-suppressed EEG signal as:

$$\mathbf{W}_{\text{SSP}}\mathbf{Y}(t) \approx \mathbf{W}_{\text{SSP}}\mathbf{L}\mathbf{J}(t) + \mathbf{W}_{\text{SSP}}\mathbf{M}_{\text{N}}\mathbf{S}_{\text{N}}(t)\,. \tag{9}$$

The downside of SSP is that it also distorts the neuronal topographies (Mäki and Ilmoniemi, 2011). Again, this is analogous to rejecting bad channels; as we discard specific signal directions to suppress artifact signals, the image of the data changes. However, this change is somewhat intuitive for channel removal, and we can easily interpolate the missing channels for data visualization. On the contrary, when rejecting muscle-artifact topographies from EEG, the changes in the EEG projection of brain activity are more abstract. Furthermore, we often visualize EEG with topographical plots, which directly connect to the physical world; the colors at the electrode locations correspond to the measured voltages. After SSP, we lose such intuition since the rows of EEG no more represent any specific EEG channels. Instead, each row of the data matrix corresponds to a linear combination of the original channel signals. Thus, to recover the physical intuition of EEG after SSP, we need to interpolate the rejected abstract signal directions of the data.

Source-informed reconstruction (SIR) is a technique that utilizes the forward model of the head to interpolate the signal directions removed by SSP (Mutanen et al., 2016). Although the out-projected signal dimensions might seem abstract, they are precisely defined in the $\mathbf{W}_{\text{SSP}}$ operator. This information can be taken into account when estimating the cortical brain activity $\hat{\mathbf{J}}(t)$ that produced the artifact-suppressed versions of EEG:

$$\hat{\mathbf{J}}(t) = (\mathbf{W}_{\text{SSP}}\mathbf{L})^{+}\mathbf{W}_{\text{SSP}}\mathbf{Y}(t)\,, \tag{10}$$

where $(\cdot)^{+}$ denotes pseudoinverse. A common way to construct the pseudoinverse in EEG analysis is to use minimum-norm estimation (Hämäläinen and Ilmoniemi, 1994), elaborated in the next section. With the help of the forward model, we can reconstruct the sensor signals in the original EEG channels from the artifact-suppressed current estimates; by simply multiplying the cortical current with the lead-field matrix, we obtain:

$$\hat{\mathbf{Y}}(t) = \mathbf{L}\hat{\mathbf{J}}(t)\,. \tag{11}$$

Thus, the SSP–SIR procedure can be summarized with one equation:

$$\hat{\mathbf{Y}}(t) = \mathbf{L}(\mathbf{W}_{\text{SSP}}\mathbf{L})^{+}\mathbf{W}_{\text{SSP}}\mathbf{Y}(t) = \mathbf{W}_{\text{SSP–SIR}}\mathbf{Y}(t)\,. \tag{12}$$

The principle of the combined SSP–SIR method is illustrated in Fig. 2.

Since its publication, SSP–SIR has been used in numerous TMS–EEG studies for suppressing the TMS-evoked muscle artifacts (Salo et al., 2018, 2019; Bagattini et al., 2019; Salo et al., 2020; Mancuso et al., 2021; Grasso et al., 2021; Pievani et al., 2021). In their study, (Mancuso et al., 2021) compared the performance of SSP–SIR to independent component analysis (ICA) (Korhonen et al., 2011; Rogasch et al., 2014) and observed a similar overall performance. The principal component analysis (PCA) method by ter Braack et al. (2013) is essentially a form of SSP and it would be possible to add the SIR step to reconstruct the post-PCA EEG signals in the original sensors.

The use of SSP–SIR is not limited to TMS-evoked muscle artifacts and researchers have additionally applied it to other disturbances. Depending on the problem, an appropriate strategy to isolate the artifact

[1] A good example is an ocular artifact, which contaminates several channels but is typically described by two dominating spatial patterns corresponding the horizontal and vertical movement of the eyes.

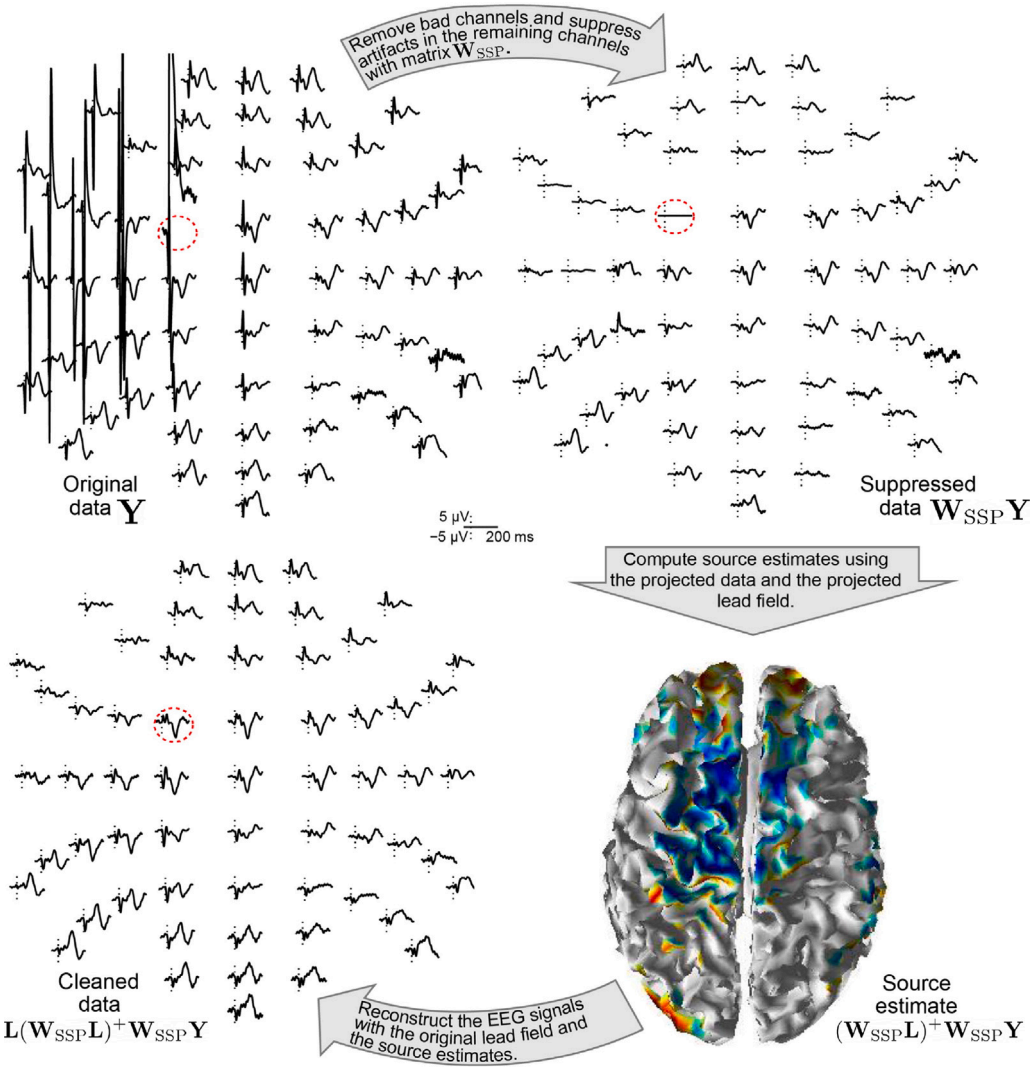

Fig. 2. The principle of SSP–SIR. Muscle artifacts are first projected out with the spatial filter $\mathbf{W}_{\mathrm{SSP}}$. By taking into account the suppressed lead-field $(\mathbf{W}_{\mathrm{SSP}})\mathbf{L}$, the muscle-artifact-suppressed data are inverted into the source space. Using the original lead-field matrix, we can project the artifact-free cortical-current estimates back to the original sensors. The figure is adapted with permission from the original work by Mutanen et al. (2016).

signals from EEG is needed. For TMS-evoked muscle artifacts, the high-pass-filtering approach has shown to work (Eqs. (7)–(8)). Vosskuhl et al. (2020) suppressed the transcranial alternating current-induced (tACS) artifact from EEG signal with SSP–SIR. Biabani et al. (2019) and Fernandez et al. (2021) have also applied the SSP–SIR approach for attenuating the TMS-related sensory artifacts (Gordon et al., 2018; Conde et al., 2019; Belardinelli et al., 2019). The SIR step has also been used to simply interpolate excluded noisy channels (Nieminen et al., 2016). The SIR-based channel interpolation is an essential step of the SOUND algorithm, and thus, will be elaborated in the next section.

4. SOUND algorithm

Although EEG has an excellent temporal resolution, its spatial specificity is relatively poor (Hedrich et al., 2017); the voltage patterns on the scalp have rather smeared, wide-spread shapes, and close-by EEG channels often pick up very similar voltage values from a cortical current source. Thus, cortical EEG signals are highly correlated across the sensors. Typically, this is considered a problem as it hampers, for instance, the EEG connectivity analysis; it is difficult to assess whether a high correlation between EEG sensors reflects genuine functionally relevant cortico-cortical connection or merely spread of the volume currents on the scalp. We can, however, exploit this property of EEG to recognize which parts of the signals are likely to originate from intracranial sources. By cross-validating the EEG sensor signals, we can deduce those signal components that are more likely to reflect extracranial sources, *i.e.*, noise. By utilizing an EEG forward model, we can improve the cross-validation accuracy as we have a model for the correlation structure between the EEG channels. We call this approach the SOurce-estimate-Utilizing Noise-Discarding algorithm (the SOUND algorithm, from now on referred to as simply SOUND) (Mutanen et al., 2018).

Let us assume that the noise covariance matrix $\mathrm{Cov}[\mathbf{M}_{\mathrm{N}}\mathbf{S}_{\mathrm{N}}(t)] = \Sigma_{\mathrm{N}}$ is known and stationary, *i.e.*, it does not change as a function of time. Furthermore, we have no prior knowledge for the source covariance, *i.e.*, $\mathrm{Cov}[\mathbf{J}(t)] = \lambda'\mathbf{I}$. We can then estimate the source waveforms by the standard minimum-norm estimate (Hämäläinen and Ilmoniemi, 1994) with the noise covariance as the regularization term:

$$\hat{\mathbf{J}}(t) = \mathbf{L}^{\mathrm{T}}(\mathbf{L}\mathbf{L}^{\mathrm{T}} + \lambda\Sigma_{\mathrm{N}})^{-1}\mathbf{Y} = \mathbf{P}_{\mathrm{MNE}}\mathbf{Y}(t)\,, \tag{13}$$

where $\mathbf{P}_{\mathrm{MNE}}$ is the spatial filter operator retrieving source waveform estimates and λ is the free regularization parameter.

If we knew the noise covariance matrix, we could insert it into (13) and use the source estimate as an intermediate result for the data cleaning by:

$$\hat{\mathbf{Y}}(t) = \mathbf{L}\hat{\mathbf{J}}(t) \tag{14}$$

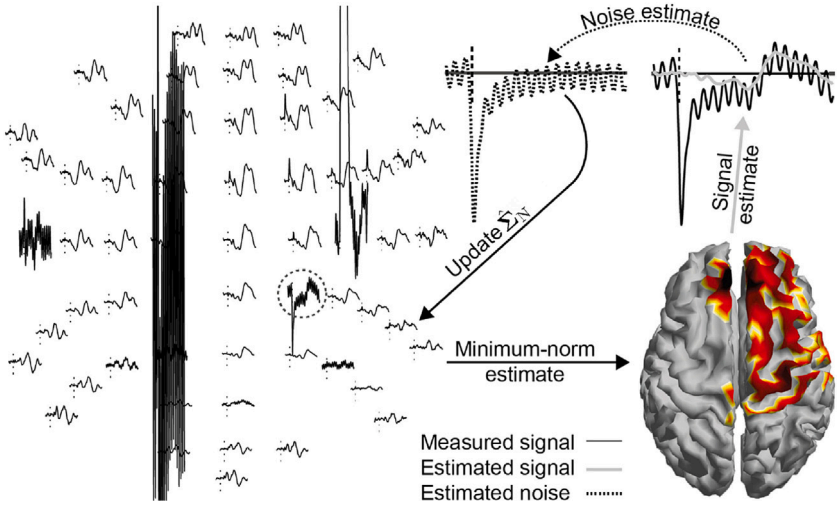

Fig. 3. The principle of the SOUND algorithm. The reliability of each channel is evaluated by cross-validating the channel against the other EEG channels. Here, we quantify the noise level of the channel of interest (CHOI; the circled channel). By computing MNE based on the other channels, we obtain an estimate for the cortical primary current. We estimate the noiseless signal in CHOI based on the obtained primary-current estimate. The difference between measured and estimated signals in CHOI is interpreted as noise. The noise covariance matrix is updated to take into account the noise level of CHOI. When evaluating the noise levels of the remaining channels, the algorithm already knows that CHOI is relatively noisy and weighs its signal less in MNE. Adapted with permission from Mutanen et al. (2018).

We aim to use the above-described cleaning to eliminate noise that is uncorrelated over channels and with the brain signals, which arises, *e.g.*, due to poor electrode contacts or artifact phenomena arising in the electrode–skin interface. We can model such noise by setting its mixing matrix to the identity matrix, $\mathbf{M}_\mathrm{N} = \mathbf{I}$, meaning that each channel has a local 'noise source'. The noise covariance matrix becomes a diagonal matrix, $\Sigma_\mathrm{N} = \mathrm{diag}(\sigma_1, \ldots, \sigma_C)$. For the noise covariance matrix, we only need to estimate the diagonal elements as sample variances of the estimated noise:

$$\hat{\sigma}_i = \frac{1}{T}\sum_{t=1}^{T} \hat{S}_{\mathrm{N},i}(t)^2 \qquad (15)$$
$$\hat{S}_{\mathrm{N},i}(t) = Y_i(t) - \hat{Y}_i(t)\,.$$

To estimate the clean signal in channel i, we proceed in the same manner as with SSP–SIR, by setting the outprojected signal dimension as the single-channel measurement at a time. The projection matrix becomes $\mathbf{W}^{(i)} = [\mathbf{e}_1, \ldots \mathbf{e}_{i-1}, \mathbf{e}_{i+1}, \ldots, \mathbf{e}_C]^\mathrm{T}$, where $\mathbf{e}_j$ is the $C \times 1$ standard basis vector having zeros at all entries except for the jth one. In practice, multiplying a target matrix from the left with $\mathbf{W}^{(i)}$ corresponds to eliminating the ith row of the target matrix.

We iterate over all the channels several times. At each channel i, the projection matrix $\mathbf{W}^{(i)}$ is applied to the linear model Eq. (5). Then, using the modified linear model for the inverse computation Eq. (13), we get:

$$\mathbf{P}^{(i)}_\mathrm{MNE} = (\mathbf{W}^{(i)}\mathbf{L})^\mathrm{T}(\mathbf{W}^{(i)}\mathbf{L}(\mathbf{W}^{(i)}\mathbf{L})^\mathrm{T} + \mathbf{W}^{(i)}\Sigma_\mathrm{N}\mathbf{W}^{(i)\mathrm{T}})^{-1}\mathbf{W}^{(i)}\,. \qquad (16)$$

After estimating the clean signal by (14), the noise level estimate is updated according to Eq. (15).

To summarize, the SOUND algorithm proceeds through an iterative process as follows (see also Fig. 3 for illustration):

1. Initialization: Set the noise covariance using initial guesses for the channel noise levels $\{\hat{\sigma}_1, \ldots, \hat{\sigma}_C\}$. Set the maximum number iterations to R, and the current iteration count to zero.
2. Increase the current iteration count by one. Update the noise variance values over all channels by repeating the following once over each of the channels:
   - For channel i, compute the estimated source signal $\hat{\mathbf{J}}$ by applying Eq. (16) to the data.
   - Estimate the cleaned signal with Eq. (14).
   - Compute $\hat{\sigma}_i$ with Eq. (15).

   See Section 7.1 for computational innovations to efficiently perform a SOUND iteration step.
3. If the estimates $\hat{\sigma}_i$ have not converged or the current iteration count does not exceed R, repeat step 2. Otherwise, proceed to step 4.
4. Final data cleaning is performed by Eqs. (13) and (14) using all of the channels and their corresponding noise estimates in the diagonal noise covariance matrix, reducing to:

$$\hat{\mathbf{Y}}(t) = \mathbf{L}\mathbf{P}_\mathrm{MNE}\mathbf{Y}(t) = \mathbf{W}_\mathrm{SOUND}\mathbf{Y}(t)\,. \qquad (17)$$

The SOUND-based single-channel iteration step corresponds to the optimal Wiener estimation result. Moreover, assuming the diagonal noise covariance, this Wiener estimate can also be obtained using only the data and the second-order statistics (covariance) of the data. The data-driven version, DDWiener (see details in Section 8.1), efficiently cleans perfectly uncorrelated EEG. In contrast, SOUND is also capable of cleaning noise that has modest cross-correlation values across the channels as long as the spatial distribution does not resemble the cross-correlation patterns predicted by the lead-field, *i.e.*, $\mathbf{L}\mathbf{L}^\mathrm{T}$ (Mutanen et al., 2018). DDWiener is a straightforward way to estimate initial guesses of the noise levels to start the SOUND iterations. It can also be used to automatically evaluate the quality of the signals and decide which channels and trials should be rejected. See further information in Section 8.1.

In practice, Eq. (13) is implemented in the open-source MATLAB implementations (Mutanen et al., 2020) and in the original article (Mutanen et al., 2018) through a different strategy where the data and lead field were whitened with respect to the noise covariance:

$$\hat{\mathbf{J}}(t) = \tilde{\mathbf{L}}^\mathrm{T}(\tilde{\mathbf{L}}\tilde{\mathbf{L}}^\mathrm{T} + \lambda\mathbf{I})^{-1}\tilde{\mathbf{Y}}\,, \qquad (18)$$

where $\tilde{\mathbf{L}} = \Sigma_\mathrm{N}^{-1/2}\mathbf{L}$ and $\tilde{\mathbf{Y}} = \Sigma_\mathrm{N}^{-1/2}\mathbf{Y}$. This formulation allows a more straightforward setting of the regularization parameter $\lambda = \lambda_0\tilde{\mathbf{L}}\tilde{\mathbf{L}}^\mathrm{T}/C$, where λ_0 is a heuristic tuning scalar. Setting the regularization level will be further discussed in Section 6.3.

SOUND has gradually gained more and more TMS–EEG applications (Ramakrishnan et al., 2019; Bagattini et al., 2019; Cline et al., 2021; Grasso et al., 2021; Zazio et al., 2021; Bortoletto et al., 2021; Fernandez et al., 2021; Mancuso et al., 2021). Because SOUND is not exclusively designed for TMS–EEG analysis but can be applied to EEG/MEG data in general, it has been used also in MEG (Rodríguez-González

et al., 2019, 2020, 2021) and (non-TMS) EEG studies (Bai et al., 2021) as a preprocessing tool. Interestingly, SOUND has been recently tested as a noise-reduction tool in the real-time studies, which can suffer from inherently low signal-to-noise ratio compared to event-related study designs (Rodríguez-González et al., 2019; Makkonen et al., 2021; Bai et al., 2021).

5. Multiple-source approach

A closely related approach to SSP, the multiple-source approach (MSA), (Berg and Scherg, 1994) was adapted by Litvak et al. (2007) to isolate the early TMS-related artifacts from the neuronal signals of interest. Instead of entirely projecting out contaminated artifact topographies $\mathbf{M}_\mathrm{A}$ by SSP, one can alternatively aim at modeling the waveform $\mathbf{S}_\mathrm{A}(t)$ that describes the temporal behavior of the underlying artifact. To this aim, all mixing matrices in Eq. (5) are concatenated horizontally into mixing matrix $\mathbf{M}$ and all the waveform matrices vertically into $\mathbf{S}$ the respective order yielding

$$\mathbf{Y}(t) = [\mathbf{L}, \mathbf{M}_\mathrm{A}] \left[\mathbf{J}(t)^\mathrm{T}, \mathbf{S}_\mathrm{A}(t)^\mathrm{T}\right]^\mathrm{T} = \mathbf{MS}(t)\,. \tag{19}$$

In practice, the neuronal lead-field matrix $\mathbf{L}$ is constructed as described in Section 2 for a fixed number of equivalent dipoles. The original work used nine brain sources distributed around the brain (Litvak et al., 2007). The artifact-mixing matrix $\mathbf{M}_\mathrm{A}$ can be formed, *e.g.*, by decomposing a data segment consisting of mostly artifacts with SVD. The first column vectors of the SVD-provided $\mathbf{U}$ form $\mathbf{M}_\mathrm{A}$ as in SSP.

Now, we may use, *e.g.*, the pseudoinverse of $\mathbf{M}$ to estimate the time-courses:

$$\hat{\mathbf{S}}(t) = \mathbf{M}^{+}\mathbf{Y}(t)\,, \tag{20}$$

from which we specifically wish to pick the estimate $\hat{\mathbf{S}}_\mathrm{A}(t)$. Finally, the artifact removal is simply evaluated as the subtraction

$$\hat{\mathbf{Y}} = \mathbf{Y} - \mathbf{M}_\mathrm{A}\hat{\mathbf{S}}_\mathrm{A}(t)\,. \tag{21}$$

The benefit of this approach is that the mixing matrix (topographies) of the neural data of interest is not modified; no interpolation of the lost signal dimensions is required post-cleaning. However, MSA may turn out impractical since the topographies (both neural and artifactual) are not known accurately enough to model the respective time courses reliably. Within TMS–EEG data, muscle artifact amplitudes can be around 100–1000 times larger than neural EEG amplitudes (Korhonen et al., 2011; Mutanen et al., 2013). For this reason, even small leakage from the remaining artifact after cleaning will lead to unsatisfactory results. In summary, MSA is expected to work well when the underlying topographies are known accurately (preferably both neural and artifactual), and the relative amplitude of the artifact with respect to the neural EEG is of moderate size.

6. Practical considerations

Getting started with SSP–SIR and SOUND is nowadays straightforward because open-source code and corresponding documentation are available (Mutanen et al., 2020). However, the effective and reliable use of these methods requires careful consideration of several practical aspects. In this section, we cover some source-based-methods-related methodological issues and their solutions.

6.1. Unbiased comparison across datasets

Oftentimes, we are not interested in the absolute amplitudes of TMS–EEG responses in one condition. Instead, we wish to compare the TMS–EEG responses in a repeated-measures design between two conditions. For instance, we might measure the same subjects in the morning and in the evening to evaluate the circadian effects on the responsiveness to TMS. In general, it is hard to assess with certainty whether the artifacts and noise have been removed perfectly. On the other hand, the neuronal signals of interest might suffer from filtering-caused overcorrection. Thus, we must be careful to not introduce any spurious differences between the conditions by applying slightly different cleaning to the compared conditions.

It is straightforward to apply SSP–SIR such that both compared datasets are cleaned identically. With SOUND, the situation is a bit more subtle. Here, we describe three typical comparison cases and how the source-based methods should be theoretically used to ensure reliable inferences; comparison within-subject between different TMS conditions, comparison within-subject between identical TMS conditions, and comparison between groups.

Let us compare two datasets where the stimulation parameters have changed. If possible, the most natural approach is to estimate the artifact and noise distributions from both datasets separately and clean both datasets with the combinations of the filters. A natural example of this type of analysis is comparing the TMS–EEG responses between different stimulation sites. Moving the stimulation target is known to modulate the TMS-evoked muscle artifacts considerably (Mutanen et al., 2013). Suppose one of the stimulation sites evokes significantly larger muscle artifacts. In that case, there is a risk that more components need to be removed in the high-amplitude-artifact condition in the SSP, resulting in a greater degree of overcorrection of the neuronal EEG signals. Let us imagine two datasets with identical noise, but different underlying neuronal responses $\mathbf{J}$ and muscle artifacts $\mathbf{A}$:

$$\begin{aligned}\mathbf{Y}^1(t) &= \mathbf{L}\mathbf{J}^1(t) + \mathbf{N} + \mathbf{A}^1\\ \mathbf{Y}^2(t) &= \mathbf{L}\mathbf{J}^2(t) + \mathbf{N} + \mathbf{A}^2\,.\end{aligned} \tag{22}$$

By applying SSP–SIR separately to both datasets as presented in Section 3 we obtain:

$$\begin{aligned}\hat{\mathbf{Y}}^1(t) &= \mathbf{L}(\mathbf{W}^1_\mathrm{SSP}\mathbf{L})^{+}\mathbf{W}^1_\mathrm{SSP}\mathbf{Y}^1(t) \approx \mathbf{L}(\mathbf{W}^1_\mathrm{SSP}\mathbf{L})^{+}\mathbf{W}^1_\mathrm{SSP}(\mathbf{L}\mathbf{J}^1(t) + \mathbf{N})\\ \hat{\mathbf{Y}}^2(t) &= \mathbf{L}(\mathbf{W}^2_\mathrm{SSP}\mathbf{L})^{+}\mathbf{W}^2_\mathrm{SSP}\mathbf{Y}^2(t) \approx \mathbf{L}(\mathbf{W}^2_\mathrm{SSP}\mathbf{L})^{+}\mathbf{W}^2_\mathrm{SSP}(\mathbf{L}\mathbf{J}^2(t) + \mathbf{N})\end{aligned} \tag{23}$$

Even if we find significant differences by contrasting $\hat{\mathbf{Y}}^1$ to $\hat{\mathbf{Y}}^2$ we cannot know whether these differences are introduced due to genuine difference between $\mathbf{J}^1$ and $\mathbf{J}^2$ or due to the different spatial filters $\mathbf{W}^1_\mathrm{SSP}$, $\mathbf{W}^2_\mathrm{SSP}$. Luckily, this is straightforward to fix; we simply apply both SSP filters to both of the datasets and obtain:

$$\begin{aligned}\hat{\mathbf{Y}}^1(t) &\approx \mathbf{L}(\mathbf{W}^1_\mathrm{SSP}\mathbf{W}^2_\mathrm{SSP}\mathbf{L})^{+}\mathbf{W}^1_\mathrm{SSP}\mathbf{W}^2_\mathrm{SSP}(\mathbf{L}\mathbf{J}^1(t) + \mathbf{N})\\ \hat{\mathbf{Y}}^2(t) &\approx \mathbf{L}(\mathbf{W}^1_\mathrm{SSP}\mathbf{W}^2_\mathrm{SSP}\mathbf{L})^{+}\mathbf{W}^1_\mathrm{SSP}\mathbf{W}^2_\mathrm{SSP}(\mathbf{L}\mathbf{J}^2(t) + \mathbf{N})\end{aligned} \tag{24}$$

Now, provided that the muscle artifacts have been suppressed sufficiently, any possible difference between the cleaned datasets $\hat{\mathbf{Y}}^1$ and $\hat{\mathbf{Y}}^2$ is due to a genuine difference in the cortical currents (when identical noise between the conditions is assumed). Note that if the muscle artifacts actually turned out to be the same in the compared conditions, we can still safely use Eq. (24), since in such a case, $\mathbf{W}^1_\mathrm{SSP}\mathbf{Y} = \mathbf{W}^2_\mathrm{SSP}\mathbf{Y} = \mathbf{W}^1_\mathrm{SSP}\mathbf{W}^2_\mathrm{SSP}\mathbf{Y}$. This approach was used successfully in Vosskuhl et al. (2020) where event-related potentials were compared during and without applying tACS, which is notorious for inducing large artifact signals to EEG (Helfrich et al., 2014).

If we are interested in within-subject comparisons between identical TMS conditions, the muscle artifacts can often be assumed equal, and we should take a different SSP strategy. By merging and averaging the compared datasets together and using that combined dataset to find the muscle artifact dimensions, we maximize signal-to-noise ratio (SNR) in the muscle artifacts and potentially improve the accuracy of the artifact estimation process. Once the common muscle artifacts have been estimated, the two datasets will be cleaned separately with the same SSP–SIR filter.

When the stimulation parameters vary between the compared conditions or the compared datasets are measured in different sessions, also the noise distribution across the channels likely differs between the conditions. This should be acknowledged when cleaning the datasets with SOUND before the qualitative or statistical comparison. Compared to SSP, the situation here is a more subtle because SOUND does not

project out the artifactual dimensions completely. Instead, it estimates the noise variances across the EEG channels to smoothly weigh them in calculating the noise-free cortical-current estimates, and thus, the final noise-free channel time courses. While SOUND detects extracranial signals effectively, it tends to smear the cortical topographies slightly. Thus, even if the noise distribution would remain the same, two consecutive SOUND operations could result in a greater degree of overcorrection, and we cannot write a similar identity for SOUND as for SSP; *i.e.*, in general, $\mathbf{LP}^1_{\mathrm{MNE}}\mathbf{Y} \neq \mathbf{LP}^1_{\mathrm{MNE}}\mathbf{LP}^2_{\mathrm{MNE}}\mathbf{Y}$. On the other hand, one of the strengths of SOUND is that, at least in principle, it allows for comparison between two conditions in channels that have been contaminated in only some conditions. For instance, a similar technique has been used to extrapolate single-channel magnetocardiography (MCG) data to the sensors signals measured by a multichannel MCG device. This approach allowed to compare single and multichannel MCG devices directly with each other (Numminen et al., 1995). The same SOUND parameters, including the regularization parameter and the number of iterations, should be used. Furthermore, the reference channel for the SOUND-iteration phase should be selected consistently across the compared datasets.

If the noise distribution can be assumed similar across the compared datasets, the most beneficial way might be to estimate the channel noise levels using the merged dataset. An example of such an experiment might be comparing two conditions, both measured in the same recording session, across the same subject. For instance, TEPs could be recorded at rest or during the task (see, *e.g.*, Nikulin et al. (2003)). If the noise distribution across the channels truly remains the same, applying SOUND to the merged dataset should allow the most reliable noise-level estimates as both the TMS-evoked neuronal signals and noise are measured with maximal SNR or deterministic-noise-to-random-noise-fluctuations ratio. This approach also ensures that regarding SOUND, the compared datasets will be cleaned identically.

For the last case, where two independent groups are compared, addressing the discrepancies between SSP–SIR and SOUND cleaning is the most challenging. If the subjects of different groups can be assumed to come from the same underlying population, a sufficient number of subjects will wash out possible variability in the subject-specific data-cleaning outcomes in the final test statistics. However, suppose the subjects or patients come from different populations, *e.g.*, a patient group vs. age-matched controls. In that case, one must carefully consider whether there is a risk that noise or muscle artifacts are different across the compared datasets.

In many cases, the source-based artifact-cleaning methods allow a straightforward way to ensure an identical correction of the compared datasets, and thus, non-biased contrasting. However, it is worth noting that sometimes this is achieved with the price in the overall signal amplitude; the more consecutive spatial filters are stacked, the more the underlying neuronal signals are compromised. If the artifacts and noise differ between the compared conditions, it might be advisable to rather over- than undercorrect the datasets. As we have shown, overcorrection can often be controlled for. However, it is impossible to control for differences in the residual artifact because this is generally not known.

6.2. Quantitative evaluation of potential overcorrection

We often lack the hard ground truth to evaluate how successfully the data cleaning removed the unwanted signal disturbances. This often forces us to visually and heuristically evaluate the cleaned data to determine whether the remaining data seem to have mainly neuronal origin. However, we can objectively evaluate the possible overcorrection for linear spatial filters such as SSP–SIR and SOUND. With *overcorrection*, we refer to unwanted suppression or distortion of the signals of interest. With the help of forward modeling, we can answer the question: Provided these cortical regions were active, how much did SOUND and/or SSP–SIR attenuate the EEG signals generated by the cortical sources of interest?

Forward modeling means the numerical estimation of the spatial EEG patterns (often referred to as topographies) generated by all the possible neuronal signal sources. While, in reality, the cortical post-synaptic currents, generating EEG, are most likely distributed, we often model them as several focal current sources; we assume that any distributed brain activity can be described in terms of a linear combination of individual current sources. The computed topographies of individual sources can be organized into matrix columns to form the lead field matrix $\mathbf{L}$, describing the sensitivity of EEG sensors to all possible cortical sources. After applying a spatial filter $\mathbf{W}$, the lead-field matrix becomes:

$$\mathbf{L}_{\text{After filter}} = \mathbf{W}_{\text{filter}}\mathbf{L}, \tag{25}$$

where "filter" can stand for SOUND, SSP–SIR, or any other linear spatial filter that maps the N-sensor EEG signal onto a set of N cleaned sensors.

The level of undesirable attenuation and distortion in the neuronal topography of a focal source i can be quantified by comparing the column vector i of the lead-field matrix before $\left(\mathbf{L}^{(i)}\right)$ and after cleaning $\left(\mathbf{L}^{(i)}_{\text{After filter}}\right)$. We can apply any meaningful measure(s) to evaluate the level of distortion, but here we focus on four classic tools. Obviously, the selected measures should quantify the type of distortion that is relevant to the research question at hand.

The amplitude difference measure ΔA_i quantifies the change in the overall amplitudes of the EEG signals of a focal unit current source i

$$\Delta A_i = \frac{\|\mathbf{L}^{(i)}_{\text{After filter}}\| - \|\mathbf{L}^{(i)}\|}{\|\mathbf{L}^{(i)}\|}, \tag{26}$$

where $\|\cdot\|$ denotes the Euclidean vector norm. Ideally, we wish ΔA_i to be as close to 0 as possible, whereas -1 would mean that the source i has lost all of its amplitude. Typically, Eq. (26) gets only negative values as the spatial filtering methods tend to attenuate cortical signals.

To measure the similarity of the shape of the EEG topographies of a source i before and after filtering, we can use the correlation coefficient (CC_i).

$$\mathrm{CC}_i = \frac{\mathbf{L}^{(i)}_{\text{After filter}} \cdot \mathbf{L}^{(i)}}{\|\mathbf{L}^{(i)}_{\text{After filter}}\| \, \|\mathbf{L}^{(i)}\|}. \tag{27}$$

Naturally, the CC values vary between -1 to 1, a value close to 1 indicating that the topographical shape of source i has remained practically unaltered.

An index ϵ_i, used to measure the relative difference between filtered and non-filtered topographies, can be computed:

$$\epsilon_i = \frac{\|\mathbf{L}^{(i)}_{\text{After filter}} - \mathbf{L}^{(i)}\|}{\|\mathbf{L}^{(i)}\|}. \tag{28}$$

We wish the discrepancy to be as small as possible, meaning that our goal is 0 for this metric. In contrast to CC and ΔA, ϵ is sensitive to changes in both the amplitude and the topographical shape.

Closely related to ϵ_i, the so-called goodness-of-fit (GOF) measure has been a common way to measure topographical similarity in MEG and EEG literature (Kaukoranta et al., 1986). GOF has been mainly used to verify the reliability of inverse techniques, such as dipole fitting or beamforming, but can also be used here to compare the filtered and unfiltered topographies:

$$\mathrm{GOF}_i = 1 - \epsilon_i^2 \tag{29}$$

Clearly, GOF of 1 means perfect performance, while a value close to 0 means complete deletion of a neuronal signal. Whereas ΔA_i and CC_i measure only the changes in amplitude or shape of topography i, respectively, both ϵ_i and GOF_i quantify the overall difference between the filtered and unfiltered topographies. Thus, choosing between ϵ_i and GOF_i is largely a matter of taste. However, it should be emphasized here that these measures are not comparable between different sensor geometries, including different choices of the reference in EEG.

The forward modeling of the unwanted filtering artifacts can be summarized in four steps.

1. Form the linear spatial filters $\mathbf{W}_{\text{filter}}$ (*e.g.*, $\mathbf{W}_{\text{SSP–SIR}}$ and $\mathbf{W}_{\text{SOUND}}$) using the real recorded TMS–EEG data.
2. Apply the formed spatial filters to the original lead-field matrix $\mathbf{L}$ to obtain $\mathbf{L}_{\text{After filter}}$, Eq. (25).
3. Compare all the cortical topographies before and after filtering, *i.e.*, the columns of $\mathbf{L}$ and $\mathbf{L}_{\text{After filter}}$, respectively, using the metric of your choice.
4. Visualize the results to answer the question: Supposing these cortical regions, relevant for my research question, were activated by TMS, how much would the spatial filtering methods have compromised their EEG projection?

We wish to provide an insight into the distortions and attenuations in the cortical topographies due to spatial filtering. To this end, the overcorrection measures are visualized as a function of the cortical location. Both SOUND and SSP–SIR have their characteristic ways to warp the cortical EEG signals. Because SOUND interprets those parts of each EEG-channel signal that the other channels cannot see as noise, SOUND tends to systematically overcorrect the lateral channels (Mutanen et al., 2018), which on average have fewer neighboring channels than in the center regions of the EEG cap. The forward model simulations can help identify how detrimental this effect is on the EEG signals that would originate from the ROIs. Similarly, regardless of the introduced SIR step (Mutanen et al., 2016) correcting some of the undesired impacts of SSP, SSP–SIR still tends to distort EEG signals. Especially those components that originate from cortical locations that lie underneath the TMS-activated scalp muscles are compromised. These effects are amplified along with the muscle-artifact amplitude (Salo et al., 2020); suppression of large muscle artifacts requires the removal of several muscle-artifact components, leading to greater neuronal-signal attenuation. This region-specific suppression is not, however, necessarily critical for the research question. The SSP–SIR-cleaned data could still turn out valuable if we are particularly interested in long-distance effective-connectivity patterns.

Fig. 4 shows an example of how different cortical sources are attenuated and distorted by the SSP–SIR filter when the TMS-evoked muscle artifacts have been removed. By inspecting the cortical maps, we can, for instance, deduce that if we are interested in the interhemispheric M1–M1 effective connectivity, we can safely use and analyze the cleaned data. However, if we wished to, for instance, measure the possible spreading of right M1-originated activity to the right parietal or prefrontal cortices, we would have to be more cautious in our interpretations of the results. The example dataset of this article comes from a 24-year-old female who received single-pulse TMS to the right primary motor cortex. The subject gave a written consent and the experiment was accepted by the Coordinating Ethics Committee of the Hospital District of Helsinki and Uusimaa.

Simulations with the EEG forward model can highlight possible methodological issues and help resolve them by applying the most appropriate filter parameters. In addition to quantifying the effects of SOUND or SSP–SIR on the lead field, we can also quantify how well different inverse estimation techniques work after applying the spatial filters by analyzing the point-spread and cross-talk functions of the resolution matrix corresponding to the inverse method of choice (Stenroos and Hauk, 2013; Todaro et al., 2019). This analysis is elaborated in Section 6.4.

To conclude, one benefit of the linear spatial filters is that after forming them based on the recorded data, the filters are explicitly defined. Their effects on hypothetical cortical signals can be modeled using source-based forward computations. While we still, in general, lack the ground truth that would help to identify objectively whether the artifacts have been successfully removed, we have methods to quantify the possible overcorrection of the neuronal EEG signals of interest.

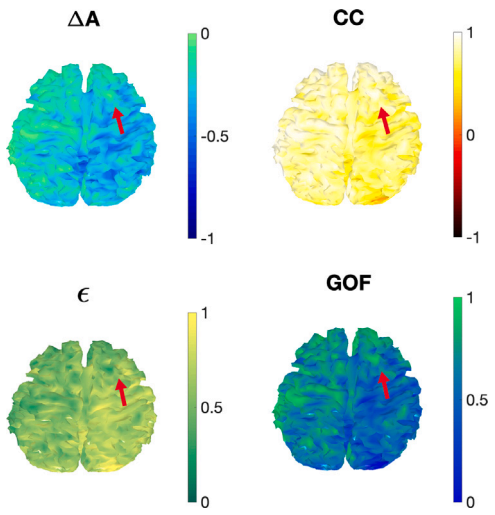

Fig. 4. An example dataset showing how the overcorrection of SSP–SIR can be quantified using forward modeling. The dataset comes from 24-year-old female who received single-pulse TMS to the right primary motor cortex. The red arrow depicts the approximate stimulation location and orientation. To suppress the initial TMS-evoked muscle artifacts, we projected out four muscle-artifact dimensions. As a result, we can observe that the signal amplitudes (ΔA) are attenuated, which is also reflected in the more general distortion measures, ϵ, and GOF. However, SSP–SIR preserves the shapes of neuronal signals well reflected in the CC map.

6.3. Optimal parameters for SOUND

While SOUND identifies noise signals with hardly any intervention by the user, there are a couple of parameters that can affect the cleaning outcome dramatically: the regularization coefficient λ in Eq. (18) and the choice of EEG reference. A larger regularization parameter in SOUND means more aggressive suppression of noise, whereas a smaller λ is a more conservative choice, meaning that the data of interest are overcorrected less, but some noise may remain after cleaning. To set the regularization to a correct ballpark, the heuristic tuning scalar λ_0 in $\lambda = \lambda_0 \tilde{\mathbf{L}}\tilde{\mathbf{L}}^\top/C$ can be chosen such that $\lambda_0 = 1/\text{SNR}$. This approach suppresses the noise more aggressively when the original SNR of the data is low.

In the original SOUND paper, we also showed a strategy for optimizing the regularization level for a given dataset to minimize the overcorrection while maximizing the SNR of the cleaned data (Mutanen et al., 2018). SNR should be estimated with some SOUND-independent metric, such as by comparing signal power at low and high frequencies. As a measure of overcorrection, we have used the correlation between the SOUND-estimated noise and neuronal time courses; the more SOUND removes signals of interest, the more the cleaned signal will correlate with the estimated noise.

A potential approach that needs validation in the future could be to assume that an EEG dataset contains at least some non-contaminated channels. After the channel-specific noise estimates have been obtained through the SOUND iterations, the user could set a tolerance level for unnecessary suppression of the best-quality channel signals. A stricter tolerance would mean less overcorrection in the good-quality channels and less aggressive cleaning of the overall noise, and *vice versa*.

The open-source implementation of SOUND (Mutanen et al., 2020) also allows the straightforward interpolation of visually identified "bad" channels based on the minimum-norm estimates derived from the "good" channels (Nieminen et al., 2016). If this is the primary use of SOUND, then the regularization level should be kept relatively low to minimize the unnecessary suppression of the good-quality channel signals.

Also the choice of the reference channel can affect cleaning outcome. It is noteworthy that the noise captured by the reference electrode is spread to all EEG channels, measuring the voltage with respect

to the reference. This makes the reference noise correlated over the channels, contradicting with the assumption of uncorrelated noise. Therefore, the reference channel cannot be cleaned efficiently with SOUND, and the noise spread among the channels by the referencing cannot be eliminated. In practice, a low-noise electrode should be chosen as the reference. The same reference should be then used in the lead-field matrix. Furthermore, suppose one is interested in analyzing the data in a particular reference system. In that case, it is favorable to transform the data and lead fields to the reference of interest already before SOUND (as long as that reference channel initially had high-quality signal). Re-referencing the data before SOUND minimizes the distortions in the neuronal signals in the reference of interest.

6.4. Artifact rejection and inverse estimation

The analysis of TMS-evoked EEG has been largely based on analyzing and visualizing the sensor-space signals (see, *e.g.*, Nikulin et al., 2003; Daskalakis et al., 2008; Veniero et al., 2013; Premoli et al., 2014). For such applications, SSP–SIR and SOUND are useful methods that are rather straightforward to use when distilling the genuine cortical signals from the noisy measurements. However, from the beginning of TMS–EEG, one of its main applications has been the estimation of cortical effective connectivity (Ilmoniemi et al., 1997; Massimini et al., 2005; Ferrarelli et al., 2010; Bagattini et al., 2019), which in practice requires source estimation. Thus, it is essential to understand how the source-based noise-cancellation methods should be applied when source-estimation is of primary interest. On the other hand, even with the best practices, noise and artifact cancellations always compromise the signals of interest. Therefore, it is necessary to understand how the source estimates are affected by the applied methods. This section demonstrates, through simple simulations, how to use best spatial filtering with inverse estimation to ensure reliable current estimates.

Here, we concentrate on the inverse-estimation technique, standardized low-resolution brain electromagnetic tomography (sLORETA) (Pascual-Marqui et al., 2002), which has also been used with TMS–EEG data (Ragazzoni et al., 2013; Bagattini et al., 2019). sLORETA serves as an excellent example because it has a specific theoretical characteristic; in ideal conditions, the location of the maximum amplitude of a source estimate corresponds to the actual location of the underlying focal source (Pascual-Marqui et al., 2002). As we will demonstrate, this property is broken if the spatial filtering is inadequately taken into account. The straightforward principles presented here can be, however, easily applied to minimum-norm estimation (MNE) (Hämäläinen and Ilmoniemi, 1994) or beamforming (Van Veen et al., 1997).

The characteristics of different inverse techniques can be analyzed by quantifying the properties of the so-called resolution matrix (Hauk et al., 2019; Todaro et al., 2019; Hauk et al., 2022). The resolution matrix describes the linear relationship between the true and estimated cortical sources. In practice, the resolution matrix is formed by first applying the inverse-estimator $\mathbf{G}$ of interest to the measured data (Eq. (5)) to find the estimate $\hat{\mathbf{J}}$ for the cortical currents. The inverse operator $\mathbf{G} \equiv \mathbf{G}_\mathbf{L}$ is a function of the lead-field matrix $\mathbf{L}$. Even in the absence of noise and artifacts, Eq. (5) does not have a unique solution for $\mathbf{J}$. Thus, the exact formulation of $\mathbf{G}_\mathbf{L}$ depends on the underlying assumptions and the chosen optimization problem (Hauk and Stenroos, 2014) that produces a unique solution. The estimated currents $\hat{\mathbf{J}}$ can be written:

$$\hat{\mathbf{J}}(t) = \mathbf{G}_\mathbf{L}\mathbf{L}\mathbf{J}(t) + \mathbf{G}_\mathbf{L}\mathbf{M}_\mathrm{A}\mathbf{S}_\mathrm{A}(t) + \mathbf{G}_\mathbf{L}\mathbf{M}_\mathrm{N}\mathbf{S}_\mathrm{N}(t)\,, \tag{30}$$

where $\mathbf{R} = \mathbf{G}_\mathbf{L}\mathbf{L}$ is the resolution matrix. The ith row of $\mathbf{R}$ is a so-called cross-talk function (CTF), which describes how much the other cortical sources "leak" to the estimate of a focal source i. On the other hand, the ith column of $\mathbf{R}$ corresponds to the point-spread function (PSF) of source i, *i.e.*, how the source estimate of a focal source i spreads to the locations of other sources. By inspecting how the CTFs and PSFs behave with the TMS–EEG data cleaning, we get precious insight on how the inverse-estimation is affected by the spatial filtering. For sLORETA, $\mathbf{G}_\mathbf{L}$ can be written (Hauk et al., 2019; Todaro et al., 2019; Hauk et al., 2022):

$$\mathbf{G}_\mathbf{L} = \mathrm{diag}(\mathbf{P}_\mathrm{MNE}\mathbf{L})^{-1/2}\mathbf{P}_\mathrm{MNE}\,, \tag{31}$$

where $\mathrm{diag}(\mathbf{X})$ is a diagonal matrix having the diagonal values of matrix $\mathbf{X}$.

The most straightforward way to perform source analysis is to apply SSP–SIR and SOUND to produce noise-attenuated versions of the TMS-evoked neuronal EEG signals and use these as a starting point when inverse-estimating the cortical activity. However, as we already pointed out in Sections 6.1 and 6.2, after applying a spatial filter to the data, the relationship between the cortical current sources and sensor signals changes. In practice, this means that instead of the original lead field $\mathbf{L}$, the new post-filtering lead-field $\mathbf{W}_\mathrm{filter}\mathbf{L}$ is a more accurate representation of the mapping of the cortical activity onto EEG signals (Eq. (25)). If the use of the spatial filters is not taken into account in the inverse estimation, the resulting resolution matrix is $\mathbf{R} = \mathbf{G}_\mathbf{L}\mathbf{W}_\mathrm{filter}\mathbf{L}$. However, because the spatial filter is known, we can use the updated lead field to find the inverse estimator, and the resulting resolution matrix is $\mathbf{R} = \mathbf{G}_{\mathbf{W}_\mathrm{filter}\mathbf{L}}\mathbf{W}_\mathrm{filter}\mathbf{L}$.

We analyzed the properties of the resolution matrices using two different metrics, the peak localization error (PLE) and spatial dispersion (SD). PLE of PSF is intuitive and quantifies the error between the location of the maximum estimated current and the true location of the focal current source if only that source would have been active. In the ideal case of no noise and perfectly known lead fields, this error is zero for sLORETA by definition (Pascual-Marqui et al., 2002). However, in the real world, the brain is likely to have multiple sources active simultaneously. PLE of CTF quantifies the distance between the source of interest i and the source that leaks the most to the estimate of i if the whole cortex would be equally active. Ideally, both PLE of PSF and CTF would be 0. SD of PSF quantifies the spread of the current estimate when only the focal source in question has been active. On the other hand, SD of CTF quantifies the extent of the cortical area from which the other sources leak to the activity estimate of the source of interest.

Fig. 5 shows the properties of (the resolution matrix of) sLORETA in three different conditions. The *Standard* condition refers to a situation where no spatial filtering has been applied to the data. In the *Post SSP–SIR* condition, SSP–SIR has been used to suppress TMS-evoked muscle artifacts when the right primary motor cortex has been stimulated with 90% of the motor-threshold intensity. In total, seven artifact dimensions have been removed by SSP. However, this operation has not been taken into account when forming the sLORETA estimator $\mathbf{G}$. Finally, in the *SSP-optimized* condition, the original lead-field matrix has been replaced with the filtered version of the lead-field matrix when forming $\mathbf{G}$. Note that the SIR correction is not needed when computing the inverse estimates and is sufficient only to perform the SSP step. Correspondingly, the lead-field matrix $\mathbf{L}$ is replaced with $\mathbf{W}_\mathrm{SSP}\mathbf{L}$.

Overall, different conditions produce subtle differences in the PSFs and CTFs. As expected, sLORETA shows overall small PLE values in PSFs, whereas CTFs reflect significant leakage between different sources, which is typical for EEG. SD is high in general, related to the low spatial specificity of EEG. However, when the different conditions are compared to each other (Fig. 6), it is clear that using the SSP–SIR-cleaned data directly with sLORETA does not produce optimal results. However, taking SSP into account in the SSP-optimized condition returns the 0-PLE for PSFs. Furthermore, while also SSP-optimized sLORETA increases SD of PSFs, the situation is substantially better than in the Post-SSP–SIR condition. The changes in CTFs were small compared to their overall PLE and SD values. Not surprisingly, SSP–SIR introduced problems mainly to the stimulated (right) side. This is since the removed muscle artifact topographies overlap more with the neuronal topographies from this side.

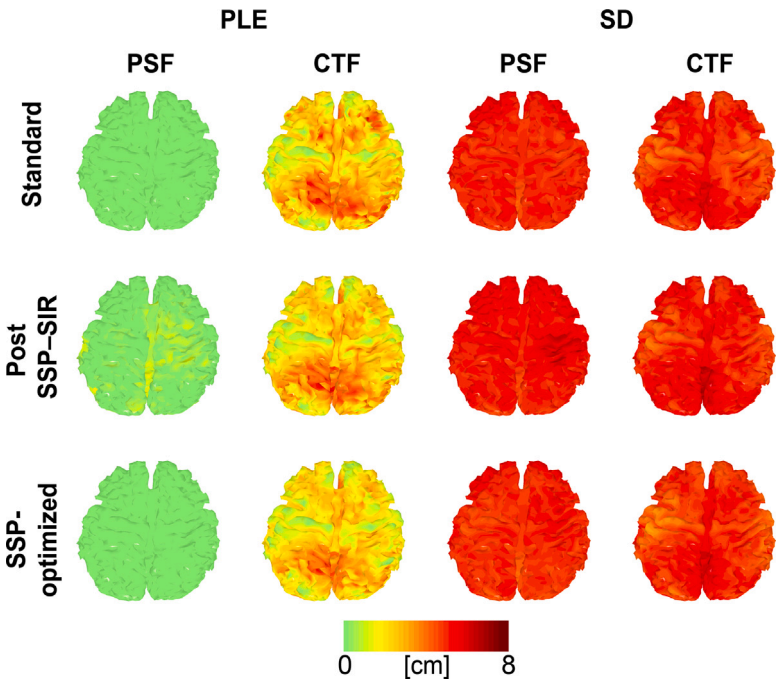

Fig. 5. The performance of sLORETA with different filtering approaches. Different columns show the PLE and SD values of PSFs and CTFs. The Standard condition row demonstrates a situation where no spatial filtering has been needed. The Post SSP–SIR row shows what happens when the SSP–SIR-cleaned data has been fed directly to standard sLORETA. The SSP-optimized row shows the correct way to combine SSP with sLORETA. See Fig. 6 for contrast between the conditions.

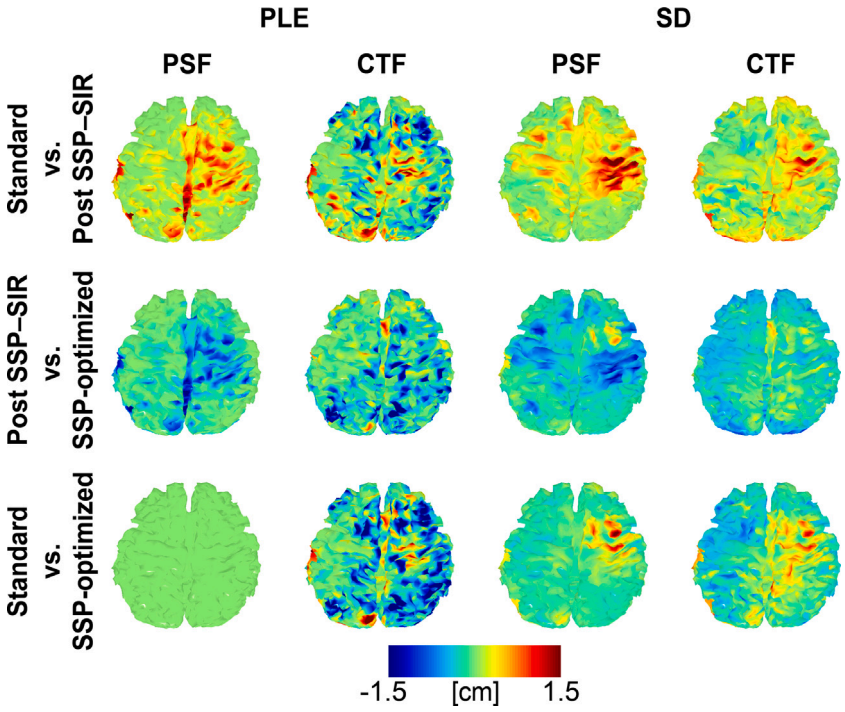

Fig. 6. Contrasting the sLORETA performances in different filtering conditions. Top row: Compared to standard condition, when no SSP is needed, the direct use of post-SSP–SIR data in sLORETA clearly increases PLE of PSF and SD of both PSF and CTF in the stimulated hemisphere. Mid row: Taking SSP correctly into account in the sLORETA inverse operator (SSP-optimized condition) decreases both PLE and SD compared to post-SSP–SIR condition. Bottom row: Even after SSP artifact rejection, the zero-localization error of sLORETA can be recovered with the SSP-optimized approach (PLE of PSF). However, SSP still compromises SD of both PSF and CTF.

6.5. Requirements for the forward model

An essential part of applying the source-based methods is to construct the forward model (or lead-field matrix) that is used as prior to either detect noise signals, as in SOUND (Mutanen et al., 2018), or to reconstruct the artifact-free signals in the original sensor space, as in the SIR step (Mutanen et al., 2016). The original logic that led to SSP–SIR and SOUND was based on estimating the noise- and artifact-free cortical currents, which could be used to interpolate the missing signal-space directions (*e.g.*, see Figs. 2–3). However, it turns out that both methods can be written in terms of lead-field covariance matrices $\mathbf{C_L} = \mathbf{L}\mathbf{L}^{\mathrm{T}}$. This means that instead of mapping accurately topographies

of the actual cortical postsynaptic sources, it is sufficient that the used forward model depicts accurately the typical cross-correlations between EEG channels, in the presence of neuronal activity.

Because it is only required that the chosen forward model accurately depicts the lead-field-covariance, we can achieve successful data cleaning with simplified head models. Both SOUND and SSP–SIR have been successfully applied using only a three-layer spherical model (Mutanen et al., 2016, 2018). Hence by default, the open-source SSP–SIR and SOUND functions construct and apply the three-layer spherical models, based on the theoretical 10–20 EEG-channel locations, unless the user provides a more detailed lead field among the input parameters (Mutanen et al., 2020).

Nonetheless, an anatomically more accurate forward model has been shown to perform better, particularly in SOUND (Mutanen et al., 2018). For instance, inaccuracies in the head geometry lead to overcorrection, especially on the lateral sides of the head. Due to the real curvature of the head, a simple spherical head model does not capture perfectly the cross-correlation between the lateral and other channels. However, moderate errors in the applied conductivity values did not dramatically affect the performance of SOUND (Mutanen et al., 2018). This is reassuring as the exact conductivity values of the different head tissues are still not perfectly known (Vorwerk et al., 2019). If possible during experiments, the scalp location of the reference channel should also be measured for the construction of the lead field. This allows calculating the forward model in the original reference and operating SOUND to the data in its original reference. Otherwise, an intermediate step is needed to transform the data and lead-field to the same reference before SOUND. Such an intermediate step increases the risk that the noise in the used reference signal is spread over all the channels, making the noise irremovable by SOUND.

6.6. Cleaning TEPs with SSP–SIR and SOUND

When preprocessing TMS–EEG data, a common question is raised: What other preprocessing steps should be combined with SOUND and SSP–SIR and what is the optimal order for the data-cleaning steps? In general terms, one should apply as little cleaning and filtering to the data as possible to avoid overcorrecting the data, hindering the final interpretations. If the artifacts within the time window of interest are suppressed simply by the application of SOUND or SSP–SIR (with just a few removable components), one should refrain from further correction. In practice, this is often not enough: When TEPs are highly artifactual, several consecutive cleaning steps are taken to get a satisfactory result (Bertazzoli et al., 2021). Here, we discuss how to perform the multi-step cleaning and the beneficial preprocessing actions before SOUND or SSP–SIR.

SOUND assumes uncorrelated noise, so the preprocessing prior to SOUND should enhance the noise uncorrelatedness and not create additional correlations. Slow-frequency drifts are general phenomena, which arise at the single-channel level (not from the brain or environmental disturbances). Still, they can appear spatially spread because the dataset recording times are not long enough to compute representative covariance matrices of such slow disturbances. High-pass filtering or detrending is therefore beneficial. We also recommend setting the signal offset at each channel to zero to prevent biased EEG activity maps affecting the noise-level estimates.

As discussed, the used reference signal is spread over all the channels, making the noise in this reference spatially correlated and not removable by SOUND. We further note that any spatial filtering mixes the EEG noise somehow, creating correlations, and hampering SOUND performance. The mixing into each channel i from the original data can be checked from the ith row of the filter matrix. This fact would be in favor of performing SOUND before other spatial filtering steps.

SOUND has two opposing effects on the consecutive SSP–SIR as explained in the following. On the other hand, after SOUND, the spatial maps underlying EEG have been smoothened by applying the correction matrix $\mathbf{W}_{\mathrm{SOUND}}$. If any artifacts remain, they have also been smoothened as $\mathbf{W}_{\mathrm{SOUND}}\mathbf{M}_{\mathrm{A}}$ according to Eq. (5), which means that they have become increasingly overlapping with the SOUND-smoothened neural topographies, *i.e.*, the columns of $\mathbf{W}_{\mathrm{SOUND}}\mathbf{L}$. This can bring along challenges since SSP preserves neural data best when there is minimal overlap (correlation coefficient) between the neural and the artifactual topographies. This problem is alleviated by the fact that, commonly, SOUND alone can eliminate artifacts to such extent that the number of needed SSP out-projection components decreases. As a result, the EEG dimensionality does not need to be dropped as much as when applied to the EEG before SOUND.

After choosing and estimating the pipeline order and the correction matrices, one can check how the correction affects the separability and possible attenuation of the sources using the head model as discussed in Section 6.2. Here, we show an example case of this type of analysis by checking the source amplitude modification when SSP alone is used as compared to SOUND followed by SSP–SIR. In this case, SSP is applied with seven out-projected topographies, whereas after SOUND fewer PCA-derived topographies were out-projected to yield a desired level of artifact attenuation. SOUND was applied with three different levels of regularization, the regularization coefficient set to 0.01 (termed as low regularization), 0.1 (medium regularization), and 1 (high regularization). The higher this coefficient is, the smoother the data appears after SOUND, and the fewer out-projection components are needed for the SSP–SIR step, the numbers here being 5, 3, and 2 for the low, medium, and high regularization levels, respectively. The regularization values here refer to the tuning scalar λ_0 in Eq. (18).

For the above-described four settings, we investigated the remaining relative source power p_i^{source}, which for source i was defined as:

$$p_i^{\mathrm{source}} = \sqrt{\frac{\|\mathbf{W}\mathbf{L}_i\|^2}{\|\mathbf{L}_i\|^2}}, \tag{32}$$

where $\mathbf{L}_i$ is the ith lead-field matrix topography, and $\mathbf{W}$ is the used total spatial filter matrix, *i.e.*, it combines both SOUND and/or SSP(–SIR) depending on how they were used.

Results are summarized in Fig. 7. Overall, when the regularization coefficient in SOUND is increased, the area on the cortex, where the source power is remarkably diminished, gets enlarged: With small regularization, focal cortical patches near the stimulation target and on the contralateral area are damped down, while medium regularization clearly makes these areas more diffuse. The focal attenuation of contralateral activity is actually produced by SOUND alone (not depicted here), which indicates that there are probably no source signals with good SNR arising in this contralateral area. The difference between the regularization levels is also seen in the histogram (bottom in Fig. 7), where it also shows that large regularization provides clear overall attenuation, and it should probably be avoided. In this example case, SSP alone seems to silence only a relatively small area near to the TMS target, as seen in Fig. 7 on top left, coinciding with the dark patch with small regularization. In the histogram, we see that combined SOUND+SSP–SIR with small regularization spreads the distribution of the remaining source power, meaning that there are sources whose power either increases or decreases, as compared to SSP alone.

The type of evaluations presented here can be easily performed for individual datasets to make the final decisions of pipeline designs. When performing group-level analysis after preprocessing, common pipelines are oftentimes required. Again, we stress that one should always compare the pipelines from the viewpoint of the study at hand: Not all brain activity may be relevant, in which case the source attenuation in uninteresting cortical regions should not be taken into consideration.

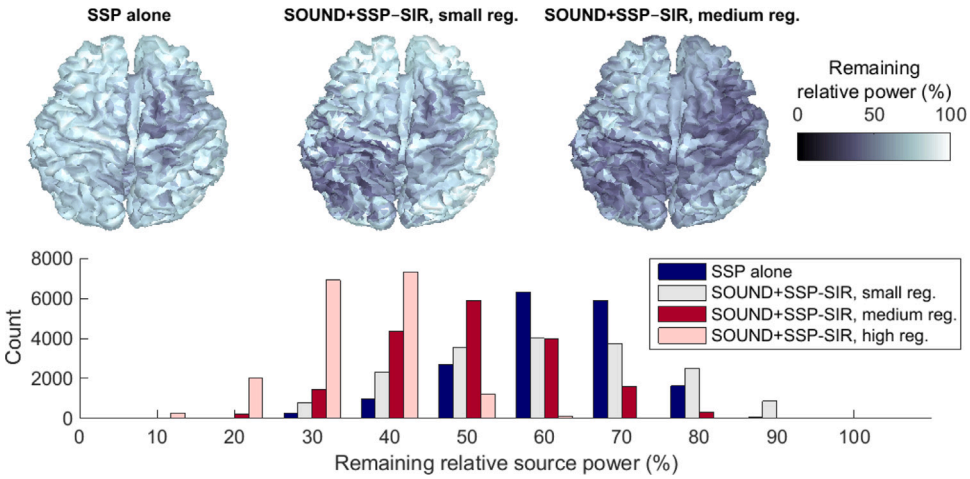

Fig. 7. The relative remaining source power was computed by Eq. (32) in three scenarios using SSP and SOUND followed by SSP–SIR. Different regularization coefficients were used: 0.01 (assumed SNR = 100), 0.1 (assumed SNR = 10), and 1 (assumed SNR = 1) are referred to as 'small reg.', 'medium reg.' and 'high reg.', respectively. Top: Distributions depicted on the cortical surface. Bottom: Histogram showing the overall distributions regardless of the anatomical cortical locations for comparison across the cleaning types.

6.7. Cleaning individual TMS–EEG trials

Not all TMS–EEG analysis relies on averaging the responses over trials, although averaging is beneficial from the noise attenuation perspective. As trial-to-trial variability is attenuated by averaging, also noise is diminished simultaneously. For instance, TMS-induced oscillations are studied by analyzing the power (variance) of the random-phase EEG signals within different frequency bands (Pellicciari et al., 2017). In addition, single-trial-level cleaning is also valuable for drawing statistical links between EEG responses and some other measure (Niessen et al., 2021), or for example, as a preprocessing step prior to blind-source-separations methods (Metsomaa et al., 2014), which require lots of input data.

For the types of analyses making advantage of unaveraged data, the usage of the SSP–SIR and SOUND may be different from the averaged TEP analysis: When averaging as a noise-suppressing step is not included, the regularization term in SOUND or the number of eliminated components in SSP–SIR may need to be increased to obtain a sufficiently clean outcome. Such heavier cleaning, on the other hand, may result in attenuation of the neural signal of interest, so a compromise may be needed. If any prior knowledge of the locations or frequencies of the sources of interest is available, this information could be used in the correction methods to preserve the sources of interest as well as possible. At the same time, the artifacts would be suppressed at the cost of eliminating less relevant source activity. In practice, the prior knowledge could be incorporated in the source covariance matrix in MNE. In SSP, the artifact topographies should be estimated from a frequency band that overlaps minimally with the studied frequency band.

7. Recent advancements

7.1. Enhancing the computation of SOUND

Two simple innovations have significantly enhanced the computation of SOUND and made some applications more feasible in practice, including the time-adaptive SOUND (Section 7.2), the real-time SOUND (Section 7.3), and the cleaning individual trials separately.

First, regardless of how the lead field has been computed, we recommend to replace the actual lead field, which may consist of thousands of columns, with a singular-value-decomposition-based square matrix as follows:

$$\begin{aligned}\mathbf{L} &= \mathbf{U}\mathbf{S}\mathbf{V}^{\mathrm{T}} \\ \hat{\mathbf{L}} &= \mathbf{U}\mathbf{S}\,.\end{aligned} \tag{33}$$

This is because the equations of SOUND (Eqs. (13)–(17)) actually rely on the lead-field covariance matrix, rather than the full lead-field matrix. On the other hand, **U** and **S** matrices are sufficient for writing the covariance matrix:

$$\begin{aligned}\mathbf{C}_{\mathbf{L}} &= \mathbf{L}\mathbf{L}^{\mathrm{T}} \\ \mathbf{C}_{\mathbf{L}} &= \mathbf{U}\mathbf{S}\mathbf{V}^{\mathrm{T}}\mathbf{V}\mathbf{S}\mathbf{U}^{\mathrm{T}} \\ \mathbf{C}_{\mathbf{L}} &= \mathbf{U}\mathbf{S}\mathbf{S}\mathbf{U}^{\mathrm{T}} = \hat{\mathbf{L}}\hat{\mathbf{L}}^{\mathrm{T}}\,.\end{aligned} \tag{34}$$

Second, with large datasets, estimating noise levels from Eq. (15) is time-consuming since SOUND iterations proceed through all channels multiple times. Let us insert the definitions from Eqs. (14) and (16) into Eq. (15) to compute the noise signal as:

$$\hat{S}_{\mathrm{N},i}(t) = \mathbf{e}_i^{\mathrm{T}}\mathbf{Y}(t) - \mathbf{e}_i^{\mathrm{T}}\mathbf{L}\mathbf{P}_{\mathrm{MNE}}^{(i)}\mathbf{Y}(t) = (\mathbf{e}_i^{\mathrm{T}} - \mathbf{e}_i^{\mathrm{T}}\mathbf{L}\mathbf{P}_{\mathrm{MNE}}^{(i)})\mathbf{Y}(t) = (\mathbf{w}_{\mathrm{N}}^{(i)})^{\mathrm{T}}\mathbf{Y}(t)\,, \tag{35}$$

where we used the unit basis vector $\mathbf{e}_i$ to pick the ith column from a matrix, *e.g.*, $Y_i(t) = \mathbf{e}_i^{\mathrm{T}}\mathbf{Y}(t)$. We note that applying a spatial filter vector $\mathbf{w}_{\mathrm{N}}^{(i)}$ to the data sample vector gives the respective estimate for noise sample at channel i. Finally, using this identity to compute the noise level by Eq. (15) yields:

$$\hat{\sigma}_i = (\mathbf{w}_{\mathrm{N}}^{(i)})^{\mathrm{T}}\mathrm{Cov}(\mathbf{Y})\mathbf{w}_{\mathrm{N}}^{(i)}\,. \tag{36}$$

Using Eq. (36) allows us to efficiently update the noise levels since the data covariance matrix needs to be computed only once, after which the original data samples are not used within the SOUND iterations. One simply updates $\mathbf{P}_{\mathrm{MNE}}^{(i)}$ to update the spatial filter vector and recomputes Eq. (36). This update rule may speed up the computational time by several orders of magnitude compared to sample-wise updates, depending on the dataset size.

7.2. Time-adaptive SOUND

One statistical characteristic of TMS–EEG data is that noise is generally non-stationary; *i.e.*, the noise covariance matrix changes over time. For instance, the TMS pulse can polarize the skin–electrode interfaces of poorly connected channels, resulting in high-amplitude artifacts that easily dominate the noise covariance matrix right after the TMS pulse (Ilmoniemi and Kičić, 2010). These polarization artifacts decay exponentially, lasting from tens to a few hundred milliseconds. TEPs often contain also sustained noise signals, such as line noise or persistent muscle activity. After the possible sporadic artifacts have passed, the noise covariance matrix mainly describes the spatial patterns of such noise signals. If the noise covariance matrix is known to be highly non-stationary, the original time-invariant SOUND might

overcorrect artifactual channels also during those time points when they are relatively clean. Theoretically, the optimal solution is to clean the data in a time-adaptive way as follows.

The noise level estimate $\hat{\sigma}_{i,t}$ for channel i and time point t is computed with a slight variation of Eq. (15):

$$\hat{\sigma}_{i,t} = \frac{1}{E}\sum_{e=1}^{E} \hat{S}_{\mathrm{N},i,t}(e)^2 \qquad (37)$$
$$\hat{S}_{\mathrm{N},i,t}(e) = Y_{i,t}(e) - \hat{Y}_{i,t}(e)\,,$$

where e stands for epoch (or trial), and E is the total number of epochs. The time-dependent noise estimates can be substituted to Eq. (16) for running a separate SOUND iteration to each time point. In the time-adaptive SOUND, a very practical initial guess before time-point-specific iteration can be found from the previous time point. As a result, we form a time-dependent SOUND filter, which can be applied to individual time points in the normal way:

$$\hat{\mathbf{Y}}(t) = \mathbf{W}_{\mathrm{SOUND}}(t)\mathbf{Y}(t)\,. \qquad (38)$$

To minimize the possibility for abrupt changes in the filtering outcome between subsequent time points, the cleaned signals $\hat{\mathbf{Y}}(t)$ can be median-filtered. Another elegant solution is to base each time-point-specific noise-estimate to a set of values over an overlapping time window. This can be written:

$$\hat{\sigma}_{i,t} = \frac{1}{E}\frac{1}{T_{\mathrm{window}}}\sum_{e=1}^{E}\sum_{t_j=T_0}^{T_{\mathrm{end}}} \hat{S}_{\mathrm{N},i,t_j}(e)^2 \qquad (39)$$
$$T_0 = t - T_{\mathrm{window}}/2$$
$$T_{\mathrm{end}} = t + T_{\mathrm{window}}/2\,,$$

where T_{window} is the length of the applied time window.

The time-adaptive SOUND approach was successfully used for the first time by Bagattini et al. (2019), when they studied whether prefrontal connectivity alterations may be linked to Alzheimer's disease severity. While the initial implementation worked well, it was tediously slow. With the computational innovations, described in Section 7.1, a dataset consisting of dozens of channels, hundreds of trials, and thousands of time points is now cleaned in a matter of few minutes. The computation time can be further shortened with parallel computing.

7.3. Real-time cleaning

The recent innovations in the SOUND algorithm (see Section 7.1) have enhanced the computation so much that real-time SOUND has become feasible (Makkonen et al., 2021). Real-time correction is crucial in closed-loop TMS–EEG techniques (see Section 8), in which the brain state is used to control TMS (Zrenner et al., 2018). In addition, real-time cleaning is important in EEG-based brain-computer interface (BCI) applications (Curran and Stokes, 2003) and could potentially enhance traditional (TMS–)EEG measurements by providing information about channel-wise noise levels and their changes during an experiment.

The spatial-filter implementation of SOUND correction allows fast and straightforward noise removal by applying the filter separately to every incoming data sample in real-time. The filter can be constantly updated by reading a short data segment, to estimate the current noise covariance, and thus, to calculate the corresponding noise-removing spatial filter (see Fig. 8). The SOUND calculation does not slow down the real-time sample-by-sample process because it runs in the background as a parallel process.

The spatial filter needs to be updated as frequently as possible to reflect the changes in the noise covariance of the data. The noise covariance matrices can be updated in tens to hundreds of milliseconds, depending on the length of the data segment and the number of recorded EEG channels (Makkonen et al., 2021). The iteration process can be accelerated by using the noise estimate from the previous filter update as an initial guess. Moreover, a sliding weight change can be implemented between consecutive filters to avoid abrupt changes in the streaming data.

When using real-time SOUND in TMS–EEG, extracting only data segments that do not include TMS pulse artifacts is important. In single-pulse TMS–EEG experiments, separate filters and update processes can be used for pre-and post-pulse data because the noise covariance in post-pulse data (*e.g.*, 0–500 ms after the pulse onset) might be different due to the TMS-pulse-evoked disturbances. However, this approach must be refined in the future for multi-locus TMS (mTMS) (Koponen et al., 2018) and repetitive TMS applications (Klomjai et al., 2015), in which pulses can be delivered at a much faster rate.

In tests with streamed pre-recorded TMS–EEG data, real-time SOUND cleaning produced EEG signals similar to those cleaned with traditional offline SOUND (Makkonen et al., 2021). Qualitative results demonstrated that real-time SOUND restored signals in noisy EEG channels while leaving high-quality channels unaltered. When launching a new update every 2 s, EEG data segments as short as 1000 samples were found adequate for estimating the noise covariance of the data nearly as precisely as offline SOUND. Additionally, frequency spectra were consistent between real-time and offline SOUND-cleaned EEG data. This indicates that the method could be suitable for closed-loop use, in which determining the brain state from spontaneous EEG is important (Bai et al., 2021).

Real-time SOUND cleaning offers many benefits in addition to fast and robust noise removal. The spatial-filter-based correction pipeline allows easy addition of other spatial-filter correction methods, such as SSP–SIR. Furthermore, the quality of EEG data can be monitored in real-time by comparing consecutive noise covariance values returned by SOUND. Sudden large changes in the noise levels can be used as an indicator of temporary low data quality. Such bad data segments can be discarded until the signal quality recovers.

We have recently implemented real-time SOUND cleaning in the real-time EEG-processing architecture presented by Zrenner et al. (2018). This architecture is used for EEG-controlled TMS, in which real-time cleaning is important. In the implementation, SOUND spatial filtering was realized as a fast linear matrix operation as a part of a linear sample-by-sample process. In contrast, the slower SOUND update iteration was implemented as an asynchronous parallel process, as in Fig. 8, on a separate computer. We have also conducted preliminary experiments with real-time cleaning in the architecture to see any possible improvement in the accuracy of phase-based EEG-controlled TMS. The data from these experiments are currently being analyzed. Overall, the tentative results of real-time SOUND are promising (Makkonen et al., 2021), but further work is needed to validate the performance and reliability in the real world.

8. Future directions

8.1. General data-driven noise estimation

Often in TMS–EEG studies, we measure more multidimensional data than the number of electrodes might suggest. For instance, we repeat a particular stimulus several times to measure the evoked responses. This means that our raw data consists of at least three independent variables: sensors, time, and trials. In SOUND, we test how well the other sensors can explain and predict the signal in the studied sensor through MNE. Using this information, we can deduce sensor-specific noise estimates. The very same idea can be generalized to other measurement dimensions. This could allow the introduction of new, more objective, and efficient ways to find contaminated trials or entire datasets during preprocessing.

Let us consider a general multidimensional measurement $\mathbf{Z}(t)$

$$\mathbf{Z}(t) = \mathbf{X}(t) + \mathbf{N}(t)\,, \qquad (40)$$

which consists of the underlying true noiseless measurement of interest $\mathbf{X}(t)$ and noise $\mathbf{N}(t)$. For simplicity, t refers here to time but could stand

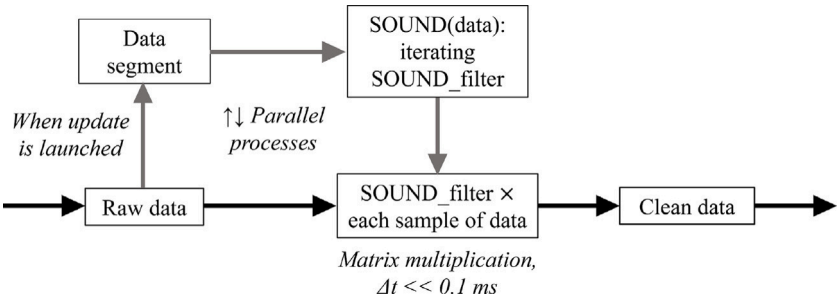

Fig. 8. The working principle of real-time EEG cleaning with the SOUND algorithm. Each raw data sample is multiplied with the SOUND spatial filter. The filter is regularly updated in a parallel process, based on short data segments. Adapted with permission from Makkonen et al. (2021).

for trials or any other dimension at which the variables have been sampled. The rows of **Z** could contain, for instance, data collected from different participants or trials. We assume that **N** is temporally uncorrelated over its elements (rows). Furthermore, **N** is assumed uncorrelated with **X**. In contrast to the noise, we assume that **X** has some correlation over its elements, but this correlation structure is not *a priori* known. We aim to estimate the true signal for the element i (*e.g.*, the ith TMS–EEG trial) linearly from the other measurements (other trials). To this end, we seek to find the linear filter $\mathbf{w}_i$ that minimizes the expected difference between the true and the best estimate for the noiseless measurement $\hat{x}_i$;

$$\hat{x}_i(t) = \mathbf{w}_i^{\top}\mathbf{W}^{(i)}\mathbf{Z}(t)\,, \tag{41}$$

where $\mathbf{W}^{(i)}$ corresponds to eliminating the ith row from the target matrix when applying $\mathbf{W}^{(i)}$ from the left, and $\mathbf{w}_i$ is obtained by minimizing the optimization problem:

$$\hat{\mathbf{w}}_i = \underset{\mathbf{w}_i}{\operatorname{argmin}} \, \|\hat{x}_i(t) - x_i(t)\|\,, \tag{42}$$

where $\|\cdot\|$ stands for the L_2-norm.

Eq. (42) can be solved by taking the derivative of the minimization expression w.r.t. **w**, yielding the well known Wiener estimator:

$$\hat{\mathbf{w}}_i = (\mathbf{W}^{(i)}\mathbf{Z}\mathbf{Z}^{\top}\mathbf{W}^{(i)\top})^{-1}\mathbf{W}^{(i)}\mathbf{Z}x_i^{\top}\,. \tag{43}$$

In general, the true measurement x_i is not known. However, as we assumed that the noise n is uncorrelated across the repetitions (*e.g.*, trials), and with the true noiseless signal x, it turns out that $\mathbf{W}^{(i)}\mathbf{Z}x_i^{\top}(t) = \mathbf{W}^{(i)}\mathbf{Z}z_i^{\top}$ and the filter can be constructed using entirely the recorded data:

$$\begin{aligned}\mathbf{W}_{\mathrm{DDWiener}} &= [\hat{\mathbf{w}}_1, \hat{\mathbf{w}}_2, \ldots, \hat{\mathbf{w}}_N]^{\top} \\ \hat{\mathbf{w}}_i &= (\mathbf{W}^{(i)}\mathbf{Z}\mathbf{Z}^{\top}\mathbf{W}^{(i)\top})^{-1}\mathbf{W}^{(i)}\mathbf{Z}z_i^{\top}\,.\end{aligned} \tag{44}$$

We call this approach the Data-driven Wiener estimator (DDWiener). DDWiener provides a useful initial guess for the SOUND algorithm. However, DDWiener can also be used to evaluate the reliability of, not only sensors, but also other dimensions, such as participants or trials. Using trials still as an example, the mean noise of the ith trial can be estimated as the difference between the original and DDWiener-cleaned signals:

$$\begin{aligned}n_i^{\mathrm{ave}} &= \frac{1}{T}\|z_i(t) - \hat{x}_i(t)\| \\ \hat{\mathbf{X}}(t) &= \mathbf{W}_{\mathrm{DDWiener}}\mathbf{Z}(t)\,,\end{aligned} \tag{45}$$

where T is the total number of time samples.

Fig. 9 illustrates how useful DDWiener can be when applied to trials. For instance, trials that contained a blink show a high noise amplitude in frontal channels. On the other hand, corrupted channels show high noise levels in all trials because of the lack of correlation across the trials.

Eqs. (44) and (45) can be applied to multiple problems in the way that is most convenient for the research question. Ultimately, different applications of DDWiener simply require the appropriate organization of the data. For instance, in Fig. 9, the trial-specific noise levels were evaluated separately for each channel. Suppose our primary interest is to evaluate the general noise level of each trial without differentiation between the channels. Then, we simply need to concatenate the multichannel data of each trial into a long vector and organize the trial data into the row vectors of a matrix. The formed data matrix can then be operated with the DDWiener filter (Eq. (44)) to find the best estimate for the noiseless measurements for each trial. The trial-specific noise level can be estimated as the root-mean-square amplitude of the difference between the original and DDWiener-cleaned trial data as in Eq. (45). On the other hand, we might wish to find, *e.g.*, outlier subjects who would fail to respond to the TMS pulse in a typical way (*i.e.*, nonresponders). Then, the subject-specific responses, such as TEPs, should be organized first into the row vectors of the operated matrix, after which we could proceed in the same way as with trials.

Even though DDWiener is a data-driven method, when applying DDWiener, one should first carefully consider what the reasoning for the prediction between the used variables would be. This is important also because overfitting of the model to the data may occur even though no true predictive phenomenon exists. In the case of cross-channel EEG modeling, we know *a priori* that the neural sources are seen by several EEG channels. For this reason, it is reasonable to 'interpolate' one missing channel based on the other ones. This interpolation is represented by the linear model using the other channels as an input by which the missing channel signal is predicted. On the other hand, if we leave one trial out and predict/interpolate the EEG within this trial using the other ones, what phenomenon is the prediction based on, and do we have some *a priori* knowledge on that? Traditionally it is thought that a single evoked EEG response is a superposition of a fixed (trial-independent) deterministic data and randomly varying 'noise' responses. Averaging is typically applied to cancel out the noise and to uncover the deterministic response. If the single-trial responses are generated in this manner, the underlying model in Eq. (40) changes such that $\mathbf{X}(t) = \mathbf{X}$ is the deterministic response independent on the trial t. It turns out that the estimate for the left-out trial given by Eq. (44) simply becomes the average of the responses from the other trials. In this case, we could not really predict the EEG based on the trial index t. On the other hand, if it is hypothesized that there are some trial-index-dependent trends in the responses, this could indeed be modeled and studied by DDWiener. Such trends would be, *e.g.*, gradual and systematic attenuation or increase in the signal amplitudes as a function of trial index. Even cyclic phenomena could be analyzed if they were to be induced by the used TMS protocol.

8.2. Artifact and noise-rejection in closed-loop EEG–TMS–EEG

While TMS has practical applications in clinical and basic research settings, the reported effects are often variable, both within and between subjects (Tremblay et al., 2019). By optimizing the target and onset of the TMS pulse based on the concurrent brain state, we could enhance the efficacy and repeatability of TMS. TMS–EEG could provide real-time information about the cortical activity with excellent

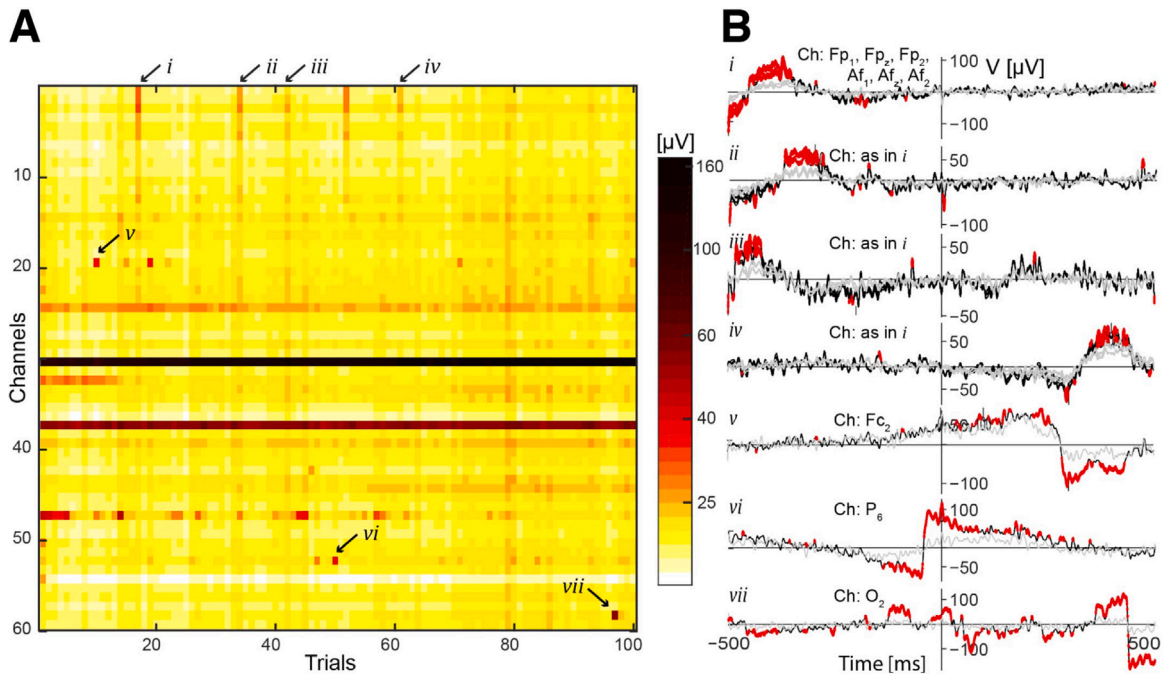

Fig. 9. DDWiener was used to estimate the noise level of each trial. **A**: The color map shows the estimated noise level at each sensor and in each trial. The arrows show the representative examples of the trials identified as highly noisy by DDWiener (*i–vii*). **B**: Time courses of noisy channels in the specific trials (*i–vii*). The black curves show the measured signals, whereas the gray curves show the corresponding DDWiener estimates. The red segments in the time courses highlight the likely reason for the high noise score in that particular trial, showing the moments when the difference between the measured and estimated signals is greater than in 99% of all the collected samples. Reprinted with the permission from Mutanen et al. (2018).

temporal resolution. However, we must manage the inherently low SNR of raw EEG for EEG-informed closed-loop TMS to be effective and adaptable for different applications. Real-time SOUND (see Section 7.3) could turn out to be a vital tool providing means for objective real-time cleaning of the data during real-time closed-loop EEG–TMS.

So far, we have tested the real-time SOUND mainly for processing streaming EEG data before TMS-pulses. However, as the closed-loop EEG–TMS–EEG techniques evolve, we might want to deliver subsequent stimuli quickly after the initial TMS pulse to impact the brain optimally. To this end, further preprocessing may be needed for, *e.g.*, suppressing the TMS-evoked muscle artifacts. Luckily, the real-time cleaning strategy presented in Section 7.3 can easily include additional spatial filters, such as SSP–SIR.

The real-time cleaning solutions serve, not only closed-loop EEG–TMS–EEG, but also other BCI applications (Benda and Volosyak, 2019). For MEG, real-time algorithms that can separate neuronal signals from external noise already exist. The signal-space separation (SSS) can detect noise signals that originate from outside the MEG sensor array based on fundamental electromagnetics (Taulu and Simola, 2006; Guo et al., 2010). SOUND provides an appealing option, especially for EEG–BCI applications. With SOUND, we can detect extracranial noise signals from EEG similarly to SSS, which can detect MEG noise signals that arrive from the outside of the sensor array.

8.3. Suppression of TMS-elicited peripheral responses

So far in the TMS–EEG framework, SSP–SIR has been mainly applied to TMS-evoked muscle artifacts. However, in principle, SSP–SIR could be applied to other artifacts as well (see *e.g.*, Vosskuhl et al., 2020), as long as the topographies of the artifacts and signals of interest differ sufficiently (Uusitalo and Ilmoniemi, 1997). Over the past few years, it has been debated to which extent the peripheral evoked potentials (PEPs) related to TMS-elicited scalp sensations and the coil-click-related auditory reactions mask the direct cortical responses to the TMS-induced electric field (Gordon et al., 2018; Conde et al., 2019; Belardinelli et al., 2019). Recently, Biabani et al. (2019) applied SSP–SIR to attenuate the impact of sensory inputs on TEPs. The artifact subspace was spanned by the few most significant principal components of PEPs evoked with sham stimuli, *i.e.*, TMS targeted to the left shoulder. While the results were partially promising, it was clear that the overall signal amplitude of TEPs was compromised during the cleaning process. This is likely due to the overall similarity between the genuine transcranial and non-transcranial responses. In contrast to the TMS-evoked muscle artifacts, here also the rejected signal components originate from the cortex. In effect, the transcranial and non-transcranial signal subspaces might overlap heavily. An appealing and straightforward solution for this problem should be tested in the future. SSP could be applied in a time-adaptive manner; instead of estimating the global signal subspace that explains the complete PEP over its whole temporal span (~300 ms), only one topography at a time could be projected out. The topography rejected at each time point would be read directly from the corresponding point in the PEP data. In practice, some sort of windowing might be necessary to ensure a smooth finish. This approach would be very close to the time-adaptive SOUND approach (Section 7.2).

8.4. Seeking the ground truth

A question that is often raised is how the source-based methods compare to other artifact- and noise-rejection algorithms, such as independent component analysis (ICA) (Korhonen et al., 2011; Rogasch et al., 2014). Indeed, a recent study by Bertazzoli et al. (2021) showed that different preprocessing pipelines produce significantly different outcomes. However, the direct comparison between, *e.g.*, ICA and SOUND or SSP–SIR is difficult because we, in general, lack the ground truth of the underlying neuronal activity. The advances in neurophysiological modeling might turn out useful in this aspect. Recently, Aberra et al. (2020) and Shirinpour et al. (2021) modeled the activation of morphologically realistic neurons under TMS. Once we can reliably model and deduce which neuronal populations are activated by TMS, we could use the novel EEG-modeling tools (Kohl et al., 2021) to simulate ground truth signals to which we could compare the different

cleaning outcomes. Until this, the source-based methods still have one clear theoretical benefit over ICA; SSP–SIR and SOUND are largely based on the electrophysiological models of the head, and they can be applied when the statistical independence between the noise and neuronal signal components cannot be assumed.

In practice, SSP–SIR, SOUND, and ICA are often used together in preprocessing pipelines to reject different artifact types. In particular, ICA has shown its utility in disentangling ocular artifacts from the rest of the EEG (Mennes et al., 2010). This could be due to the fact that ocular signals are typically more independent of the event-related neuronal responses as they also occur at random moments, not time-locked to the stimulus, such as a TMS pulse. On the other hand, for instance, SOUND struggles to remove such signal components that are correlated across the EEG channels similarly to the EEG originating from neural sources.

In typical signal-preprocessing pipelines, the different algorithms are performed independently, in a step-by-step fashion. The challenge with this approach is that the complicated processing cascades can have surprising effects on the cleaned data outcome. However, due to the lack of ground truth, it is hard to verify possible filtering artifacts that may arise from a suboptimal filtering order. Recently, Hernandez-Pavon et al. (2022) showed that all spatial artifact filters could be written in terms of a beamforming filter $\mathbf{W}_{\mathrm{A}}^{\mathrm{BF}}$, which estimates the unknown artifact time courses $\mathbf{S}_{\mathrm{A}} = (\mathbf{W}_{\mathrm{a}}^{\mathrm{BF}})^{\mathrm{T}}\mathbf{Y}$:

$$\mathbf{W}_{\mathrm{a}}^{\mathrm{BF}} = \Sigma^{-1}\mathbf{M}_{\mathrm{A}}(\mathbf{M}_{\mathrm{A}}^{\mathrm{T}}\Sigma^{-1}\mathbf{M}_{\mathrm{A}})^{-1}\,, \tag{46}$$

where Σ is the data covariance matrix and $\mathbf{M}_{\mathrm{A}}$ is the artifact mixing matrix, containing the known artifact topographies as column vectors. Once estimated, the artifacts can be subtracted from the original data. The formulation in Eq. (46) suggests that, for instance, the ICA and SSP steps could be performed simultaneously; the blink topographies could be derived from ICA, whereas a similar high-pass filtering scheme, as explained in Section 3, could be used to estimate the muscle-artifact topographies. Future work will hopefully show us whether combining ICA and source-based spatial filtering methods inside a unified spatial filter will improve the cleaning outcome.

9. Conclusion

Source-based cleaning methods are efficient tools for cleaning TMS–EEG data from muscle artifacts and other measurement noise. They rely on the anatomical and electrophysiological models of the head and neuronal EEG generators in reconstructing noise-suppressed versions of the TMS–EEG data, rather than on purely statistical assumptions. In the future, objective and analytical comparisons between source-based methods and other preprocessing algorithms are needed to define the advantages of different methods in different situations.

One major strength of the described source-based methods is that due to the linearity of the applied spatial filters, their effects on the signals of interest are straightforward to quantify. As we demonstrated, this analysis can be done both in the source and the sensor space. The presented overcorrection analysis can help in determining whether these methods fit the research question at hand.

Few simple but vital innovations in the noise-estimation of SOUND have enhanced the computation substantially, paving the way for new applications, such as real-time TMS–EEG cleaning for closed-loop stimulation and the time-adaptive SOUND that can clean TEPs without the assumptions for stationary noise.

Although this article concentrated on specifically cleaning TMS–EEG responses, SSP–SIR and SOUND can be readily applied to other EEG/MEG applications as long as the spatial patterns of studied signals disturbances differ sufficiently from the neuronal signals of interest.

Declaration of competing interest

The authors declare that they have no known competing financial interests or personal relationships that could have appeared to influence the work reported in this paper.

Data availability

The authors do not have permission to share data.

Acknowledgments

This work has been supported by the Academy of Finland (Grant No. 321631; TPM), Emil Aaltonen Foundation, Finnish Science Foundation for Technology and Economics, and the European Research Council (ERC Synergy) under the European Union's Horizon 2020 research and innovation programme (ConnectToBrain; grant agreement No 810377).

References

Aberra, A.S., Wang, B., Grill, W.M., Peterchev, A.V., 2020. Simulation of transcranial magnetic stimulation in head model with morphologically-realistic cortical neurons. Brain Stimul. 13 (1), 175–189.

Bagattini, C., Mutanen, T.P., Fracassi, C., Manenti, R., Cotelli, M., Ilmoniemi, R.J., Miniussi, C., Bortoletto, M., 2019. Predicting Alzheimer's disease severity by means of TMS–EEG coregistration. Neurobiol. Aging 80, 38–45.

Bai, Y., He, J., Xia, X., Wang, Y., Yang, Y., Di, H., Li, X., Ziemann, U., 2021. Spontaneous transient brain states in EEG source space in disorders of consciousness. NeuroImage 240, 118407.

Belardinelli, P., Biabani, M., Blumberger, D.M., Bortoletto, M., Casarotto, S., David, O., Desideri, D., Etkin, A., Ferrarelli, F., Fitzgerald, P.B., et al., 2019. Reproducibility in TMS–EEG studies: A call for data sharing, standard procedures and effective experimental control. Brain Stimul.: Basic, Transl. Clin. Res. Neuromodulation 12 (3), 787–790.

Benda, M., Volosyak, I., 2019. Peak detection with online electroencephalography (EEG) artifact removal for brain–computer interface (BCI) purposes. Brain Sci. 9 (12), 347.

Berg, P., Scherg, M., 1994. A multiple source approach to the correction of eye artifacts. Electroencephalogr. Clin. Neurophysiol. 90 (3), 229–241.

Bertazzoli, G., Esposito, R., Mutanen, T.P., Ferrari, C., Ilmoniemi, R.J., Miniussi, C., Bortoletto, M., 2021. The impact of artifact removal approaches on TMS–EEG signal. NeuroImage 118272.

Biabani, M., Fornito, A., Mutanen, T.P., Morrow, J., Rogasch, N.C., 2019. Characterizing and minimizing the contribution of sensory inputs to TMS-evoked potentials. Brain Stimul. 12 (6), 1537–1552.

Bortoletto, M., Bonzano, L., Zazio, A., Ferrari, C., Pedullà, L., Gasparotti, R., Miniussi, C., Bove, M., 2021. Asymmetric transcallosal conduction delay leads to finer bimanual coordination. Brain Stimul. 14 (2), 379–388.

ter Braack, E.M., de Jonge, B., Van Putten, M.J., 2013. Reduction of TMS induced artifacts in EEG using principal component analysis. IEEE Trans. Neural Syst. Rehabil. Eng. 21 (3), 376–382.

Buzsáki, G., Draguhn, A., 2004. Neuronal oscillations in cortical networks. Science 304 (5679), 1926–1929.

Cline, C.C., Lucas, M.V., Sun, Y., Menezes, M., Etkin, A., 2021. Advanced artifact removal for automated TMS-EEG data processing. In: 2021 10th International IEEE/EMBS Conference on Neural Engineering. NER, IEEE, pp. 1039–1042.

Conde, V., Tomasevic, L., Akopian, I., Stanek, K., Saturnino, G.B., Thielscher, A., Bergmann, T.O., Siebner, H.R., 2019. The non-transcranial TMS-evoked potential is an inherent source of ambiguity in TMS–EEG studies. NeuroImage 185, 300–312.

Curran, E.A., Stokes, M.J., 2003. Learning to control brain activity: A review of the production and control of EEG components for driving brain–computer interface (BCI) systems. Brain Cognit. 51 (3), 326–336.

Daskalakis, Z.J., Farzan, F., Barr, M.S., Maller, J.J., Chen, R., Fitzgerald, P.B., 2008. Long-interval cortical inhibition from the dorsolateral prefrontal cortex: A TMS–EEG study. Neuropsychopharmacology 33 (12), 2860–2869.

Fernandez, L., Biabani, M., Do, M., Opie, G.M., Hill, A.T., Barham, M.P., Teo, W.-P., Byrne, L.K., Rogasch, N.C., Enticott, P.G., 2021. Assessing cerebellar-cortical connectivity using concurrent TMS-EEG: A feasibility study. J. Neurophysiol. 125 (5), 1768–1787.

Ferrarelli, F., Massimini, M., Sarasso, S., Casali, A., Riedner, B.A., Angelini, G., Tononi, G., Pearce, R.A., 2010. Breakdown in cortical effective connectivity during midazolam-induced loss of consciousness. Proc. Natl. Acad. Sci. 107 (6), 2681–2686.

Gordon, P.C., Desideri, D., Belardinelli, P., Zrenner, C., Ziemann, U., 2018. Comparison of cortical EEG responses to realistic sham versus real TMS of human motor cortex. Brain Stimul. 11 (6), 1322–1330.

Grasso, P.A., Tonolli, E., Bortoletto, M., Miniussi, C., 2021. tDCS over posterior parietal cortex increases cortical excitability but decreases learning: An ERPs and TMS-EEG study. Brain Res. 1753, 147227.

Guo, C., Li, X., Taulu, S., Wang, W., Weber, D.J., 2010. Real-time robust signal space separation for magnetoencephalography. IEEE Trans. Biomed. Eng. 57 (8), 1856–1866.

Hämäläinen, M.S., Ilmoniemi, R.J., 1994. Interpreting magnetic fields of the brain: Minimum norm estimates. Med. Biol. Eng. Comput. 32 (1), 35–42.

Hauk, O., Stenroos, M., 2014. A framework for the design of flexible cross-talk functions for spatial filtering of EEG/MEG data: DeFleCT. Human Brain Mapping 35 (4), 1642–1653.

Hauk, O., Stenroos, M., Treder, M., 2019. Towards an objective evaluation of EEG/MEG source estimation methods: The linear tool kit. p. 672956, BioRxiv.

Hauk, O., Stenroos, M., Treder, M.S., 2022. Towards an objective evaluation of eeg/meg source estimation methods–the linear approach. NeuroImage 255, 119177.

Hedrich, T., Pellegrino, G., Kobayashi, E., Lina, J.-M., Grova, C., 2017. Comparison of the spatial resolution of source imaging techniques in high-density EEG and MEG. NeuroImage 157, 531–544.

Helfrich, R.F., Schneider, T.R., Rach, S., Trautmann-Lengsfeld, S.A., Engel, A.K., Herrmann, C.S., 2014. Entrainment of brain oscillations by transcranial alternating current stimulation. Curr. Biol. 24 (3), 333–339.

Hernandez-Pavon, J.C., Kugiumtzis, D., Zrenner, C., Kimiskidis, V.K., Metsomaa, J., 2022. Removing artifacts from TMS-evoked EEG: A methods review and a unifying theoretical framework. J. Neurosci. Methods 109591.

Ilmoniemi, R.J., Kičić, D., 2010. Methodology for combined TMS and EEG. Brain Topogr. 22 (4), 233–248.

Ilmoniemi, R.J., Virtanen, J., Ruohonen, J., Karhu, J., Aronen, H.J., Näätänen, R., Katila, T., 1997. Neuronal responses to magnetic stimulation reveal cortical reactivity and connectivity. Neuroreport 8 (16), 3537–3540.

Kaukoranta, E., Hämäläinen, M., Sarvas, J., Hari, R., 1986. Mixed and sensory nerve stimulations activate different cytoarchitectonic areas in the human primary somatosensory cortex SI. Exp. Brain Res. 63 (1), 60–66.

Klomjai, W., Katz, R., Lackmy-Vallée, A., 2015. Basic principles of transcranial magnetic stimulation (TMS) and repetitive TMS (rTMS). Ann. Phys. Rehabil. Med. 58 (4), 208–213.

Kohl, C., Parviainen, T., Jones, S.R., 2021. Neural mechanisms underlying human auditory evoked responses revealed by human neocortical neurosolver. Brain Topogr. 1–17.

Koponen, L.M., Nieminen, J.O., Ilmoniemi, R.J., 2018. Multi-locus transcranial magnetic stimulation—theory and implementation. Brain Stimul. 11 (4), 849–855.

Korhonen, R.J., Hernandez-Pavon, J.C., Metsomaa, J., Mäki, H., Ilmoniemi, R.J., Sarvas, J., 2011. Removal of large muscle artifacts from transcranial magnetic stimulation-evoked EEG by independent component analysis. Med. Biol. Eng. Comput. 49 (4), 397–407.

Litvak, V., Komssi, S., Scherg, M., Hoechstetter, K., Classen, J., Zaaroor, M., Pratt, H., Kahkonen, S., 2007. Artifact correction and source analysis of early electroencephalographic responses evoked by transcranial magnetic stimulation over primary motor cortex. NeuroImage 37 (1), 56–70.

Mäki, H., Ilmoniemi, R.J., 2011. Projecting out muscle artifacts from TMS-evoked EEG. NeuroImage 54 (4), 2706–2710.

Makkonen, M., Mutanen, T.P., Metsomaa, J., Zrenner, C., Souza, V.H., Ilmoniemi, R.J., 2021. Real-time artifact detection and removal for closed-loop EEG–TMS. Int. J. Bioelectromagn. 23, 12/1–4.

Mancuso, M., Sveva, V., Cruciani, A., Brown, K., Ibáñez, J., Rawji, V., Casula, E., Premoli, I., D'Ambrosio, S., Rothwell, J., et al., 2021. Transcranial evoked potentials can be reliably recorded with active electrodes. Brain Sci. 11 (2), 145.

Massimini, M., Ferrarelli, F., Huber, R., Esser, S.K., Singh, H., Tononi, G., 2005. Breakdown of cortical effective connectivity during sleep. Science 309 (5744), 2228–2232.

Mennes, M., Wouters, H., Vanrumste, B., Lagae, L., Stiers, P., 2010. Validation of ICA as a tool to remove eye movement artifacts from EEG/ERP. Psychophysiology 47 (6), 1142–1150.

Metsomaa, J., Sarvas, J., Ilmoniemi, R.J., 2014. Multi-trial evoked EEG and independent component analysis. J. Neurosci. Methods 228, 15–26.

Mutanen, T.P., Biabani, M., Sarvas, J., Ilmoniemi, R.J., Rogasch, N.C., 2020. Source-based artifact-rejection techniques available in TESA, an open-source TMS–EEG toolbox. Brain Stimul.: Basic, Transl., Clin. Res. Neuromodulation 13 (5), 1349–1351.

Mutanen, T.P., Kukkonen, M., Nieminen, J.O., Stenroos, M., Sarvas, J., Ilmoniemi, R.J., 2016. Recovering TMS-evoked EEG responses masked by muscle artifacts. NeuroImage 139, 157–166.

Mutanen, T., Mäki, H., Ilmoniemi, R.J., 2013. The effect of stimulus parameters on TMS–EEG muscle artifacts. Brain Stimul. 6 (3), 371–376.

Mutanen, T.P., Metsomaa, J., Liljander, S., Ilmoniemi, R.J., 2018. Automatic and robust noise suppression in EEG and MEG: The SOUND algorithm. NeuroImage 166, 135–151.

Nieminen, J.O., Gosseries, O., Massimini, M., Saad, E., Sheldon, A.D., Boly, M., Siclari, F., Postle, B.R., Tononi, G., 2016. Consciousness and cortical responsiveness: A within-state study during non-rapid eye movement sleep. Sci. Rep. 6 (1), 1–10.

Niessen, E., Bracco, M., Mutanen, T.P., Robertson, E.M., 2021. An analytical approach to identify indirect multisensory cortical activations elicited by TMS? Brain Stimul.: Basic, Transl., Clin. Res. Neuromodulation 14 (2), 376–378.

Nikulin, V.V., Kičić, D., Kähkönen, S., Ilmoniemi, R.J., 2003. Modulation of electroencephalographic responses to transcranial magnetic stimulation: Evidence for changes in cortical excitability related to movement. Eur. J. Neurosci. 18 (5), 1206–1212.

Numminen, J., Ahlfors, S., Ilmoniemi, R., Montonen, J., Nenonen, J., 1995. Transformation of multichannel magnetocardiographic signals to standard grid form. IEEE Trans. Biomed. Eng. 42 (1), 72–78.

Nunez, P.L., Srinivasan, R., et al., 2006. Electric Fields of the Brain: The Neurophysics of EEG. Oxford University Press, USA.

Pascual-Marqui, R.D., et al., 2002. Standardized low-resolution brain electromagnetic tomography (sLORETA): Technical details. Methods Findings Exp. Clin. Pharmacol. 24 (Suppl D), 5–12.

Pellicciari, M.C., Veniero, D., Miniussi, C., 2017. Characterizing the cortical oscillatory response to TMS pulse. Front. Cell. Neurosci. 11, 38.

Pievani, M., Mega, A., Quattrini, G., Guidali, G., Ferrari, C., Cattaneo, A., D'Aprile, I., Mascaro, L., Gasparotti, R., Corbo, D., et al., 2021. Targeting default mode network dysfunction in persons at risk of Alzheimer's disease with transcranial magnetic stimulation (NEST4AD): Rationale and study design. J. Alzheimer's Dis. (Preprint), 1–13.

Premoli, I., Castellanos, N., Rivolta, D., Belardinelli, P., Bajo, R., Zipser, C., Espenhahn, S., Heidegger, T., Müller-Dahlhaus, F., Ziemann, U., 2014. TMS-EEG signatures of GABAergic neurotransmission in the human cortex. J. Neurosci. 34 (16), 5603–5612.

Ragazzoni, A., Pirulli, C., Veniero, D., Feurra, M., Cincotta, M., Giovannelli, F., Chiaramonti, R., Lino, M., Rossi, S., Miniussi, C., 2013. Vegetative versus minimally conscious states: A study using TMS-EEG, sensory and event-related potentials. PLoS One 8 (2), e57069.

Ramakrishnan, N., Murphy, N.R., Walker, C.P., Cuellar Leal, V.A., Soares, J.C., Cho, R.Y., Selvaraj, S., 2019. Neurophysiological effect of ketamine on prefrontal cortex in treatment-resistant depression: A combined transcranial magnetic stimulation–electroencephalography study. Chronic Stress 3, 2470547019861417.

Rodríguez-González, V., Gómez, C., Hoshi, H., Shigihara, Y., Hornero, R., Poza, J., 2021. Exploring the interactions between neurophysiology and cognitive and behavioral changes induced by a non-pharmacological treatment: A network approach. Front. Aging Neurosci. 483.

Rodríguez-González, V., Gómez, C., Shigihara, Y., Hoshi, H., Revilla-Vallejo, M., Hornero, R., Poza, J., 2020. Consistency of local activation parameters at sensor-and source-level in neural signals. J. Neural Eng. 17 (5), 056020.

Rodríguez-González, V., Poza, J., Núñez, P., Gómez, C., García, M., Shigihara, Y., Hoshi, H., Santamaría-Vázquez, E., Hornero, R., 2019. Towards automatic artifact rejection in resting-state MEG recordings: Evaluating the performance of the SOUND algorithm. In: 2019 41st Annual International Conference of the IEEE Engineering in Medicine and Biology Society. EMBC, IEEE, pp. 4807–4810.

Rogasch, N.C., Thomson, R.H., Farzan, F., Fitzgibbon, B.M., Bailey, N.W., Hernandez-Pavon, J.C., Daskalakis, Z.J., Fitzgerald, P.B., 2014. Removing artefacts from TMS-EEG recordings using independent component analysis: Importance for assessing prefrontal and motor cortex network properties. NeuroImage 101, 425–439.

Salo, K.S.-T., Mutanen, T.P., Vaalto, S.M., Ilmoniemi, R.J., 2020. EEG artifact removal in TMS studies of cortical speech areas. Brain Topogr. 33 (1), 1–9.

Salo, K.S.-T., Vaalto, S.M., Lioumis, P., Ilmoniemi, R.J., 2019. Transcranial magnetic stimulation-evoked potentials after the stimulation of the right-hemispheric homologue of Broca's area. NeuroReport 30 (16), 1110–1114.

Salo, K.S.-T., Vaalto, S.M., Mutanen, T.P., Stenroos, M., Ilmoniemi, R.J., 2018. Individual activation patterns after the stimulation of different motor areas: A transcranial magnetic stimulation–electroencephalography study. Brain Connect. 8 (7), 420–428.

Shirinpour, S., Hananeia, N., Rosado, J., Tran, H., Galanis, C., Vlachos, A., Jedlicka, P., Queisser, G., Opitz, A., 2021. Multi-scale modeling toolbox for single neuron and subcellular activity under transcranial magnetic stimulation. Brain Stimul..

Stenroos, M., Hauk, O., 2013. Minimum-norm cortical source estimation in layered head models is robust against skull conductivity error. NeuroImage 81, 265–272.

Stenroos, M., Nummenmaa, A., 2016. Incorporating and compensating cerebrospinal fluid in surface-based forward models of magneto- and electroencephalography. PLoS One 11 (7), e0159595.

Taulu, S., Simola, J., 2006. Spatiotemporal signal space separation method for rejecting nearby interference in MEG measurements. Phys. Med. Biol. 51 (7), 1759.

Thielscher, A., Antunes, A., Saturnino, G.B., 2015. Field modeling for transcranial magnetic stimulation: A useful tool to understand the physiological effects of TMS? In: 2015 37th Annual International Conference of the IEEE Engineering in Medicine and Biology Society. EMBC, IEEE, pp. 222–225.

Todaro, C., Marzetti, L., Sosa, P.A.V., Valdés-Hernandez, P.A., Pizzella, V., 2019. Mapping brain activity with electrocorticography: Resolution properties and robustness of inverse solutions. Brain Topogr. 32 (4), 583–598.

Tremblay, S., Rogasch, N.C., Premoli, I., Blumberger, D.M., Casarotto, S., Chen, R., Di Lazzaro, V., Farzan, F., Ferrarelli, F., Fitzgerald, P.B., et al., 2019. Clinical utility and prospective of TMS–EEG. Clin. Neurophysiol. 130 (5), 802–844.

Uusitalo, M.A., Ilmoniemi, R.J., 1997. Signal-space projection method for separating MEG or EEG into components. Med. Biol. Eng. Comput. 35 (2), 135–140.

Van Veen, B.D., Van Drongelen, W., Yuchtman, M., Suzuki, A., 1997. Localization of brain electrical activity via linearly constrained minimum variance spatial filtering. IEEE Trans. Biomed. Eng. 44 (9), 867–880.

Veniero, D., Ponzo, V., Koch, G., 2013. Paired associative stimulation enforces the communication between interconnected areas. J. Neurosci. 33 (34), 13773–13783.

Vorwerk, J., Aydin, Ü., Wolters, C.H., Butson, C.R., 2019. Influence of head tissue conductivity uncertainties on EEG dipole reconstruction. Front. Neurosci. 13, 531.

Vosskuhl, J., Mutanen, T.P., Neuling, T., Ilmoniemi, R.J., Herrmann, C.S., 2020. Signal-space projection suppresses the tACS artifact in EEG recordings. Front. Human Neurosci. 14, 525.

Zazio, A., Miniussi, C., Bortoletto, M., 2021. Alpha-band cortico-cortical phase synchronization is associated with effective connectivity in the motor network. Clin. Neurophysiol. 132 (10), 2473–2480.

Ziegler, E., Chellappa, S.L., Gaggioni, G., Ly, J.Q., Vandewalle, G., André, E., Geuzaine, C., Phillips, C., 2014. A finite-element reciprocity solution for EEG forward modeling with realistic individual head models. NeuroImage 103, 542–551.

Zrenner, C., Desideri, D., Belardinelli, P., Ziemann, U., 2018. Real-time EEG-defined excitability states determine efficacy of TMS-induced plasticity in human motor cortex. Brain Stimul. 11 (2), 374–389.